ANNALS OF GEOPHYSICS, 69, 2026; doi:10.4401/ag-9496
OPEN ACCESS

Source Mechanisms and stress fields of the 6 February 2023 Pazarcık Mw7.7 and Elbistan Mw7.6 earthquake sequences in SE Türkiye

Ethem Görgün[*,1], Doğan Kalafat[2], Burçak Görgün[1]

(1) Istanbul University-Cerrahpaşa, Department of Geophysical Engineering, Istanbul, Türkiye
(2) Boğaziçi University, Kandilli Observatory and Earthquake Research Institute, Istanbul, Türkiye

Article history: received November 20, 2025; accepted June 16, 2026

Abstract

We investigate aftershock centroid moment tensor solutions along the Pazarcık Mw7.7 and Elbistan Mw7.6 February 6, 2023 rupture zones during the time period February 2, 2023 – November 25, 2024. Six spatial clusters of aftershock activity are analyzed specifically the Çardak Cluster (ÇC), Doğanşehir Cluster (DC), Sürgü Cluster (SC), Erkenek Cluster (EC), Pazarcık Cluster (PC) and Amanos Cluster (AC) named according to the segmentation models of the Pazarcık-Elbistan rupture zone. Based on an aftershock hypocenter catalogue restricted to events with horizontal and vertical errors <2 km, we determine fault plane solutions for 178 events. Centroid moment tensor solutions with moment magnitudes between 3.7 and 7.7 are computed by applying a waveform inversion method on data from the Kandilli Observatory and Earthquake Research Institute (KOERI) and the Disaster and Emergency Management Presidency Earthquake Department (AFAD) broadband seismic networks. The high number of moment tensors at the Pazarcık-Elbistan rupture zone could be determined only thanks to the local seismic network and allows us to resolve the local deformation pattern with unprecedented precision. Moment tensors along the Çardak, Doğanşehir, Sürgü, Erkenek and Pazarcık Clusters allow us to identify dominantly sinistral strike-slip mechanisms with normal faulting components on NE-SW trending fault planes. Moreover, moment tensors in the Amanos Cluster predominantly exhibit NE-SW extensional normal faulting but also a substantial component of strike-slip faulting. North and southeast of the Çardak Cluster we observe a high variance in stress field orientation correlated with lower Coulomb stress values. While the Pazarcık Cluster reflects a predominant sinistral strike-slip regime with normal faulting components, the Çardak Cluster further to the north that also hosted the forthcoming Elbistan Mw7.6 mainshock 9 hours after the Pazarcık Mw7.7 earthquake represents pure left-lateral strike-slip faulting. Stress tensor inversions of the aftershock focal mechanisms show rotations of the local stresses following the Pazarcık and Elbistan mainshocks. In the Pazarcık-Elbistan mainshock area, the maximum horizontal compressive stress axis is horizontally rotated clockwise by ~65° with respect to the coseismic and long-term regional stress field. Towards the northern end of the rupture where the Elbistan mainshock area is located, stress orientations are rotated clockwise steadily. We conclude that the Pazarcık earthquake caused significant stress partitioning along the rupture. The direction of stress rotation is related to the orientation of the individual fault segments like the Çardak Fault along the EAFZ.

Keywords: Aftershock; Coulomb Stress Analysis; Fault Plane Solution; Kahramanmaraş; Moment Tensor Inversion; Stress Tensor Inversion

1. Introduction

The Mw7.7 Pazarcık earthquake (EQ) occurred at 01:17:32.41 GMT on 6 February 2023 at a depth of 16 km in the Kahramanmaraş Province. Approximately 9 hours later (10:24:46.66 GMT), the Mw7.6 Elbistan earthquake occurred about 90 km to the north-northwest of the first event, at a shallower depth of 13 km. The epicenter of the Pazarcık event is located along the southern section of the left lateral strike-slip East Anatolian Fault Zone (EAFZ) (Fig. 1a) that is one of the most seismically active transform fault systems worldwide. The EAFZ extends for ~650 km from eastern Anatolia, near the Karlıova district, to the Dead Sea Fault (Fig. 1a). It forms the south-eastern boundary of the Anatolian microplate and together with the Bitlis Suture Zone (BSZ) and the North Anatolian Fault Zone (NAFZ), accommodates the relative motion between Eurasia and Arabia (Fig. 1a). In this sector, the EAFZ consists of a series of strike-slip segments as well as normal or oblique faults, the latter generally not aligned with the main fault zone and associated with local change in strike of the principal fault zone (Arpat and Şaroğlu, 1972; Jackson and McKenzie, 1984; Şengör et al., 1985; Taymaz et al., 1991; Lyberis et al., 1992; Şaroğlu et al., 1992; Westaway, 2003; Westaway, 2004; Aksoy et al., 2007; Le Pichon and Kreemer, 2010; Emre et al., 2013; Yönlü et al., 2017; Güvercin et al., 2022). The main seismotectonic structures in the epicentral region of the Pazarcık and Elbistan earthquakes are located along the southern segment of the EAFZ and, from north to south, include the Palu Segment (PaS), Pütürge Segment (PüS), Erkenek Segment (ES), Pazarcık Segment (PS) and the Amanos Segment (AS). This structural arrangement is consistent with the morphology of the Southeastern Taurus Mountain Belt. A secondary E-W to NE-SW trending branch of the EAFZ, located northwest of Pazarcık, and hosting theMw7.6 Elbistan earthquake, comprises the Sürgü (SüF), Çardak (ÇF) and Savrun (SaF) Faults. The Doğanşehir Fault (DF) lies parallel to the EAFZ but further to the west, whereas the Narlı Fault (NF), which hosted the first mainshock, is located to the east (Fig. 1b). The kinematics of these faults are consistent with the Global Positioning System (GPS) measurements indicating a westward motion of the Anatolian Block of 12-18 mm yr^{-1} with respect to Eurasia (McClusky et al., 2000; Reilinger et al., 2006; Aktuğ et al., 2016). Additional important seismotectonics structures include the Toprakkale and Yumurtalık Faults, which are subparallel to the main EAFZ shear zone (Duman and Emre, 2013).

Instrumental (since 1900) and historical seismicity in the Pazarcık-Elbistan region have been compiled by Altunel et al. (2009) and Yönlü et al. (2017) (Fig. 1c). Large earthquakes (M ≥7.0) along the EAFZ are typically characterized by left lateral strike-slip faulting mechanisms. Historical earthquakes in 1114, 1408 and 1513 occurred in the southwestern part of the EAFZ, near the location of 2023 Mw7.7 Pazarcık event. These events caused widespread damage in Eastern Anatolia and Syria (Calvi, 1941; Soysal et al., 1981; Ambraseys, 1989; Nalbant et al., 2002). Several large earthquakes (M ≥ 7.0) in the 19th century also produced surface ruptures along the EAFZ (e.g., the 1822 M7.4, 1872 M7.2, 1874 M7.2, 1874 M7.1 and 1893 M7.1 events). According to Ambraseys (1989), more than 50% of the total length of the EAFZ segments ruptured during these events (Fig. 1c). During the instrumental period (since 1900), several significant earthquakes with M < 7.0 also occurred along the EAFZ, including the 1905 M6.8 Pütürge-Malatya, 1971 M6.7 Bingöl and 2020 M6.9 Sivrice earthquakes (Kalafat et al., 2009). The Pazarcık and Erkenek segments, as well as the Narlı Fault, which ruptured during the 2023 Pazarcık earthquake, were partially activated during the 1114 and 1513 events (Ambraseys, 1989; Ambraseys and Jackson, 1998; Yönlü et al., 2017). Historical evidence indicates that these segments had not ruptured for at least ~500 years prior to 2023 and were therefore considered a seismic gap in southeastern Anatolia (Ambraseys, 1989; Fig. 1c).

The 2023 Pazarcık-Elbistan earthquake sequence has been extensively analyzed in numerous high-impact studies. Notably, Jia et al. (2023) integrated dynamic rupture modeling with stress-mediated fault interactions and reported supershear rupture for the Elbistan event. They also highlighted the role of time-dependent failure processes in explaining the ~9-hour delay between the Pazarcık and Elbistan earthquakes, demonstrating delayed rupture initiation, supershear propagation, and the importance of stress heterogeneity. Billi et al. (2024) identified supercycle behavior along the East Anatolian Fault Zone (EAFZ), linking the 2023 doublet to millennial-scale slip accumulation and proposing a ~2,000-year supercycle in which the 2023 doublet represents a phase of strain release within a broader kinematic framework. Chen et al. (2024) analyzed stress interaction across cascading sub-events and historical earthquakes. Their results indicate that: (1) the Mw7.8 Pazarcık rupture was delayed by stress shadows from historical events (e.g., 1822 events), (2) the Mw7.6 Elbistan rupture was accelerated by cumulative stress increases and triggered by the Mw7.8 event, and (3) elevated seismic hazard persists in regions such as the Elazığ-Bingöl gap and the Dead Sea Fault, emphasizing the need for preparedness.

The extensional characteristics of some events of the 2023 Pazarcık-Elbistan earthquake sequence challenges the conventional strike-slip interpretation of the EAFZ, suggesting that crustal density variations may significantly influence surface deformation. Through an integrated analysis of CMT data and aftershock observations, we investigate how these segments couple surface deformation with Coulomb stress processes, and propose a mechanism for enhanced seismicity within strike-slip fault zones.

In this study, we further assess the hazard implications of stress heterogeneity and its potential to refine seismic hazard models in southeastern Anatolia. We perform stress tensor inversion of earthquake source mechanisms to obtain a more accurate representation of the regional stress field. For this purpose, seismic waveforms recorded at local and regional distances are used to determine source parameters for 178 events (3.7 ≥ Mw ≥ 7.7) of the 2023 Pazarcık-Elbistan earthquake sequence using the waveform inversion method (Nakano et al., 2008). These results provide additional constraints on the stress field, improving kinematic models of the Pazarcık-Elbistan region and enhancing our understanding of local and regional tectonics of the EAFZ. Furthermore, we use stress tensor parameters (Vavryčuk, 2014) to compute Coulomb stress changes (Toda et al., 2011b), allowing us to characterize the spatial evolution of the Pazarcık-Elbistan earthquake sequence. Accurate determination of stress field orientations

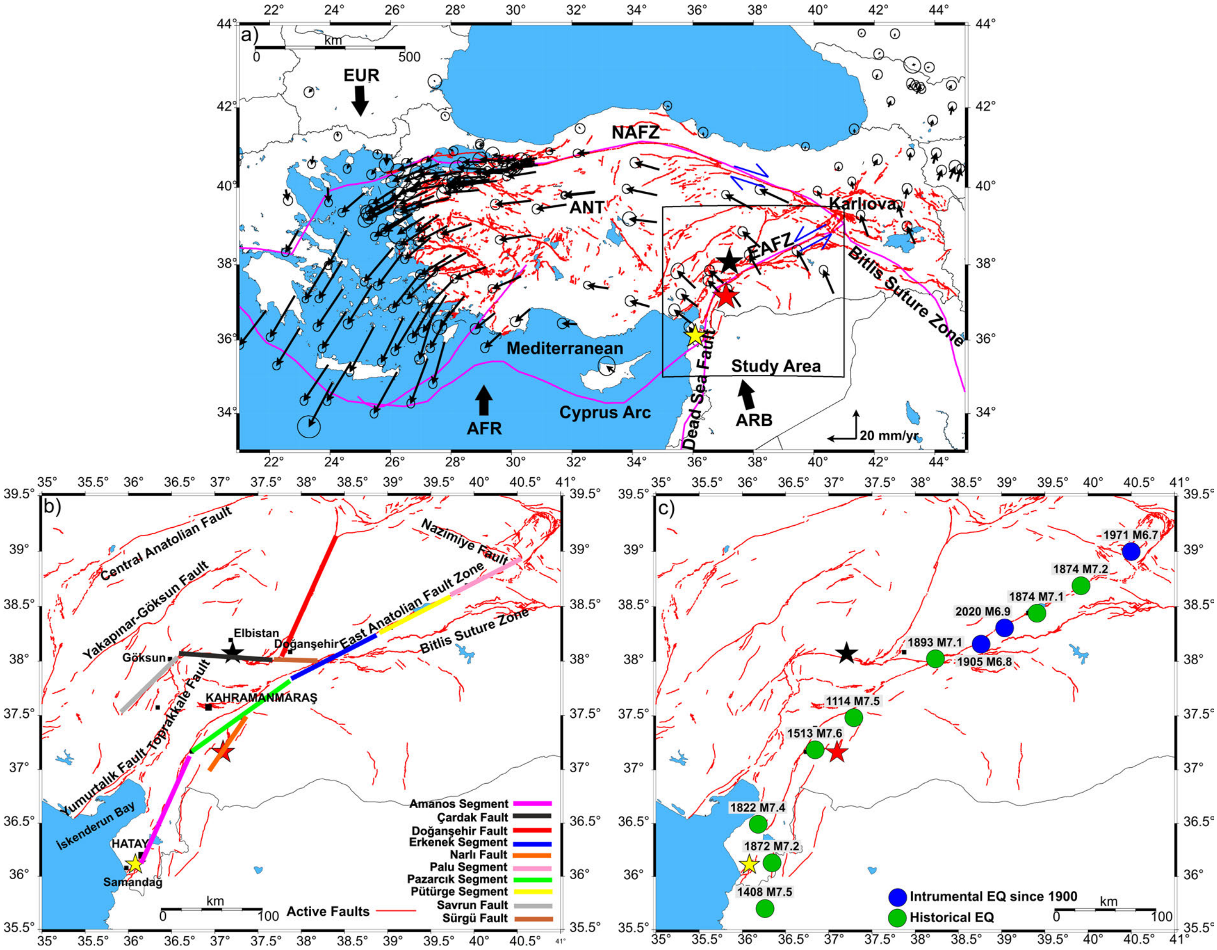

Figure 1. (a) Tectonic map of northern Aegean Sea showing GPS velocities with respect to Eurasia and 95% confidence ellipses for eastern Anatolia (McClusky et al., 2000; Reilinger et al., 2006; Aktuğ et al., 2016). Seismically active faults are shown by red lines (Şaroğlu et al., 1992; Emre et al., 2013). The epicenters of the 6 February 2023 Pazarcık Mw7.7 and Elbistan Mw7.6 EQs, and of the 20 February 2023 Samandağ Mw6.4 aftershock, are indicated by the red, black and yellow stars, respectively (same as in the following insets). Two closely spaced blue single arrows display shear sense of major faults (NAFZ: North Anatolian Fault Zone, EAFZ: East Anatolian Fault Zone). Boundaries of the Anatolian (ANT) plate, which is surrounded by the African (AFR), Arabian (ARB) and Eurasian (EUR) plates, are shown as heavy colored purple lines (Bird, 2003). The solid black rectangle shows the study area, which is enlarged in Fig. 1b and Fig. 1c. (b) Active seismotectonic segments and faults, which are indicated with different colors, and were ruptured by the Pazarcık and Elbistan mainshocks. (c) Epicenters of the previous significant historical and instrumental earthquakes (Ambraseys, 1989; Ambraseys et al., 1998; Kalafat et al., 2009). Blue and green circles exhibit instrumental (since 1900) and historical events, respectively.

and earthquake locations, based on data from local and regional seismic networks, is essential for advancing seismotectonics interpretations in the southwestern EAFZ region.

2. Data and waveform inversion method

The broadband seismic stations used in this study, operated by the Kandilli Observatory and Earthquake Research Institute (KOERI) and the Disaster and Emergency Management Presidency Earthquake Department (AFAD, are shown in Fig. 2. We selected stations with similar technical characteristics (e.g., bandwidth, sensitivity and instrument response). We used seismic records from 75 Güralp broadband stations with 100 samples/sec to perform moment tensor inversions (see Fig. 2).

Centroid moment tensor (CMT) solutions for earthquakes in the Pazarcık-Elbistan region were computed using the waveform inversion method developed by Nakano et al. (2008). In this approach, if the location corresponding to the minimum residual lies at the edge of the search area, the grid is expanded to encompass this location.

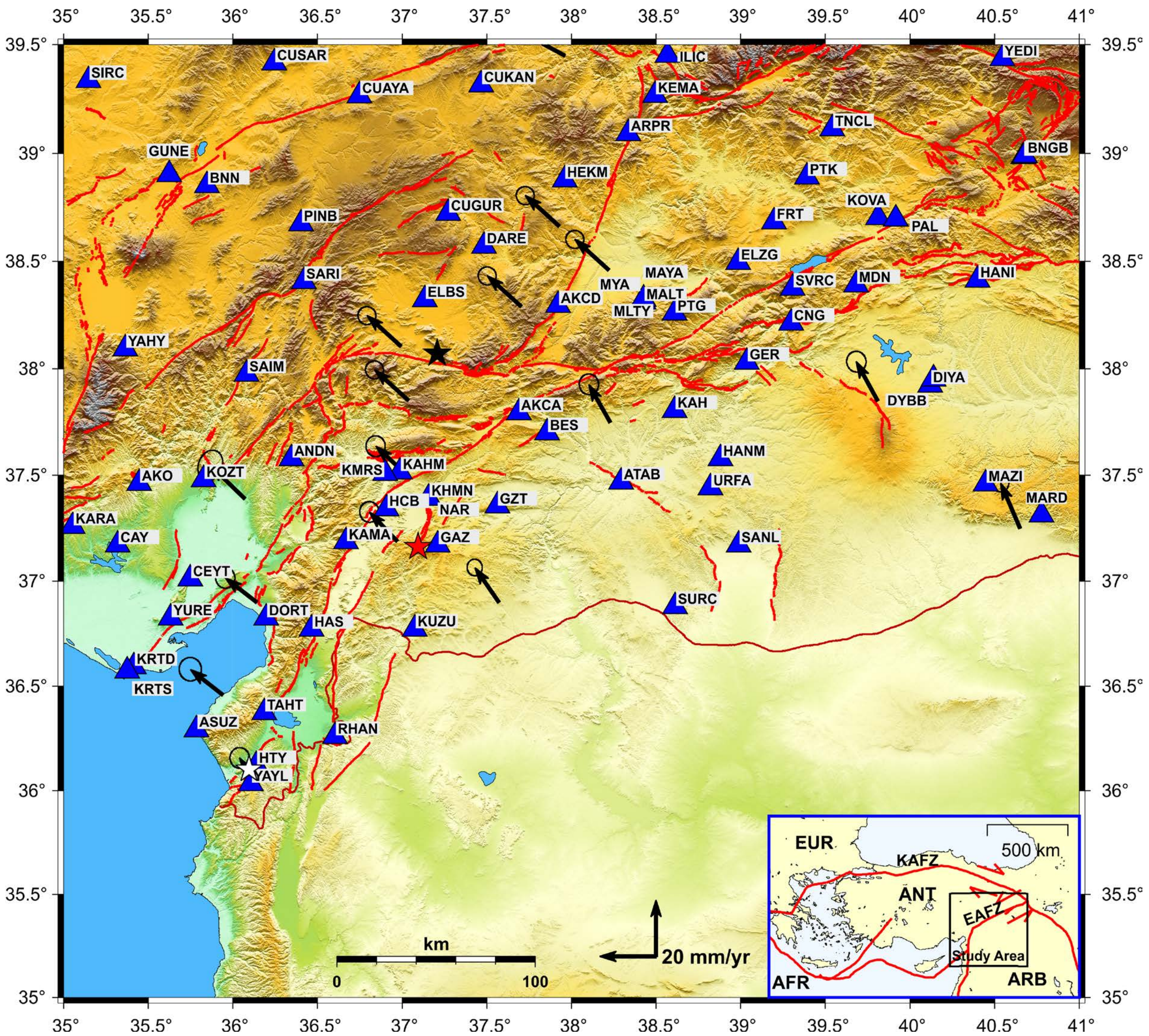

Figure 2. Blue triangles with station codes show locations of the KOERI and AFAD broadband seismic stations in topographic map view. The black arrows are GPS velocities with respect to fixed Eurasia and 95% confidence ellipses for eastern Anatolia (McClusky et al., 2000; Reilinger et al., 2006; Aktuğ et al., 2016). The inset in the bottom right shows whole Turkey region with major active faults and plate boundaries indicated by the red lines (Bird, 2003). Red, black and white stars represent the 6 February 2023 Mw7.7 Pazarcık and Elbistan Mw7.6 mainshocks and the 20 February 2023 Mw6.4 Samandağ aftershock.

Conversely, if the minimum residual is located within the search area, a new search is conducted around this point using a finer grid spacing to obtain a more precise location (Nakano et al., 2008; 2010; Görgün, 2013; Görgün, 2014; Görgün, 2015; Görgün et al., 2017; Görgün et al., 2020).

Three-component seismograms were used for the inversion of the Pazarcık-Elbistan earthquake sequence, and only seismograms with high quality data (i.e., high signal-to-noise ratio) were selected. On average, 20 three-component stations (vertical, E-W and N-S) were used for each CMT analysis. The recorded seismic data are not velocity seismograms prior to instrument-response correction. Waveforms were bandpass filtered between 20 and 50 s for events with Mw > 5.0 and decimated to a sampling frequency of 0.5 Hz. This results in reduced sensitivity to small-source characteristics (e.g., source size, rupture duration and moment tensor components). For smaller magnitude events (3.7 < Mw < 4.5), a shorter period bandpass filter of 5-20 s was applied, as these events radiate little energy at longer periods. Green's functions were generated using the discrete wavenumber method (Bouchon, 1979), based on the crustal velocity models of Ergin et al. (2004) and Ozer et al. (2019). The Ergin et al. (2004) model was preferred for the Amanos Fault region (southern part of the study region) due to its better representation of local crustal heterogeneities, particularly in complex areas such as the Hatay and Adana Basins, whereas the Ozer et al. (2019) model provides less detailed constraints on local seismic velocities (Vp and Vs). Synthetics seismograms were computed for horizontally layered structures using the two velocity models (Table 1). Green's functions were calculated for epicentral distances up to 1500 km in 10 km bins. At each distance, three-component displacements were computed at 1° azimuthal intervals for each moment tensor basis. Additionally, Green's functions were computed at 5 km depth intervals for source depths (hypocentral depth) shallower than 100 km. For spatial grid search, hypocenter locations provided by KOERI were used as initial estimates. An adaptive grid search approach was applied with progressively refined grid spacing: initially 0.5° horizontally and 10 km vertically, then 0.2° and 5 km, and finally 0.1° and 5 km. At each grid point, fault geometry parameters (strike, dip and rake) were searched in 5° increments. For each combination of source location and fault parameters, waveform inversion was performed to determine the best-fitting source model (see Nakano et al., 2008; Nakano et al., 2010 for details; Görgün, 2013; Görgün, 2014; Görgün, 2015; Görgün et al., 2017; Görgün et al., 2020). Uncertainties in the moment tensor (MT) solutions were evaluated using misfit function analysis. Following Nakano et al. (2008), we used a misfit based approach to assess focal mechanism quality and considered the azimuthal gap to evaluate station coverage. Strikes, dip and rake angles were recalculated within the 95% confidence interval and the width of this confidence interval was used as misfit measure to account for non-uniform solution distributions. This misfit factor ranges from 0 to 1, with lower values (<0.4) indicating more robust solutions. Solutions with azimuthal gaps greater than 130° or misfit values exceeding 0.4 were discarded. In Fig. 3, we show some statistics about the distribution of these parameters and the quality of the focal mechanisms obtained.

Table 1. Crustal models used to estimate the source parameters of the mainshock and its aftershocks. Vp and H are P-wave velocity and thickness of the layers, respectively.

Vp **(km s^{-1})**	***H*** **(km)**
4.60	0.0-8.0
5.80	8.0-20.0
7.40	20.0-35.0
7.90	35.0-
Özer et al. (2019).	

Vp **(km s^{-1})**	***H*** **(km)**
4.51	0.0-2.0
5.02	2.0-4.0
6.07	4.0-12.0
6.15	12.0-28.0
6.60	28.0-32.0
7.82	32.0-
Ergin et al. (2004).	

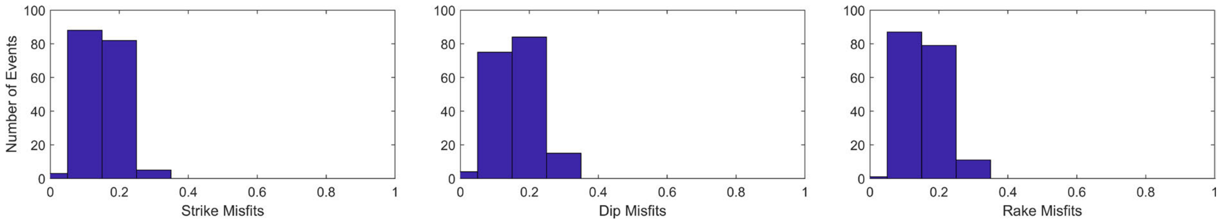

Figure 3. Histograms of the uncertainty distributions of strike, dip and rake angles for 178 focal mechanism solutions with misfits.

3. Stress tensor inversion

In this study, the technique of Vavryčuk (2014) was applied to the 178 selected events (Table 2). It uses the statistical method of bootstrap re-sampling and allows determining the orientation of the three principal stresses ($\sigma 1$ = maximum principal compressive stress, $\sigma 2$ = intermediate and $\sigma 3$ = minimum) as well as the stress/shape ratio $R = (\sigma 2 - \sigma 3)/(\sigma 1 - \sigma 3)$, also called relative stress magnitude (Bott, 1959). The R is defined using the standard geologic/geophysical notation with compressive stress positive and $\sigma 1 > \sigma 2 > \sigma 3$ (Zoback, 1992). The stress/shape ratio (R) ranges from 0 to 1. Values of $R < 0.5$ and $R > 0.5$ indicate a transpressional and transtensional regime, respectively. The uncertainties of the retrieved stress directions, the shape ratio, the fault selection and overall friction on faults are verified by the bootstrap method as proposed by Vavryčuk (2014). Here the uncertainties are calculated as the maximum differences between the results of the inversion for noise-free and noisy data with 1000 noise realizations. This method can account for cases in which some nodal planes are more uncertain than others by specifying different noise levels for the fault orientations and slip directions. In addition to this, the obtained uncertainties are more realistic. The efficiency of the iterative inversion was tested on the Pazarcık-Elbistan data. The method worked well and produced a significantly more accurate shape ratio than the inversion of the focal mechanisms with randomly selected faults.

To quantify the misfit angles (β) between the best stress tensor and the data, the angle between the calculated slip vector from stress tensor inversion and observed slip vector from fault plane solutions was used. In our study, stress tensor inversion results give β misfit angles smaller than 33°. Heterogeneity of the stress field was documented in the average β level of the inversion. For each stress inversion, 2000 bootstrap iterations are performed (Vavryčuk, 2014; Görgün et al., 2020).

Vavryčuk (2014) indicated that the principal stress directions are determined with a similar accuracy regardless of whether the faults are randomly selected from nodal planes or correctly identified by the inversion. Data with randomly selected faults yield a broad distribution of the shape ratio, with its maximum significantly biased compared to the inversion using correctly selected faults. The stress ratio (R) is more sensitive to the correct choice of the fault plane than the principal stress directions and substituting the faults by the auxiliary nodal planes introduces high errors (Lund and Slunga, 1999; Vavryčuk, 2014). The algorithm of Vavryčuk (2014) is a modified version of Michael's method (Michael, 1987) inverting jointly for stress and for fault orientations and its main advantage is that it does not suffer from incorrect use of the fault orientation which can yield wrong calculations of the shape ratio. Vavryčuk (2014) showed that the new iterative stress inversion is fast and accurate, and performs much better than the standard linear inversion. Since the iterative stress inversion is based on Michael's method, it can easily be implemented in these codes enhancing their accuracy. Vavryčuk (2014) proposed the MATLAB code of this inversion called STRESSINVERSE that is provided on the web page (http://www.ig.cas.cz/stress-inverse).

Table 2. Hypocenters and source parameters of the 2023 Pazarcık-Elbistan EQ sequence. H is hypocentral depth, Mw is moment magnitude, Str is strike angle.

No	Date	Time (GMT)	Lat (°N)	Lon (°E)	H (km)	Mw	Str (°)	Dip (°)	Rake (°)
1	03.02.2023	11:05:08.06	37.1995	36.4118	12.3	4.2	331	63	−178
2	06.02.2023	01:17:32.41	37.1613	37.0950	15.6	7.7	142	86	−165
3	06.02.2023	01:28:17.61	37.1292	36.8150	9.0	6.6	298	68	163
4	06.02.2023	10:24:46.66	38.0717	37.2063	12.7	7.6	359	79	178
5	06.02.2023	12:02:11.38	38.0697	36.4702	18.4	5.9	306	88	−174
6	06.02.2023	15:14:28.69	38.4733	37.7928	14.8	5.2	65	90	74
7	06.02.2023	16:26:36.28	38.0785	36.6955	3.8	4.8	329	87	150
8	06.02.2023	17:46:49.83	38.1987	37.8245	4.8	4.5	300	60	−60
9	06.02.2023	18:03:53.62	38.0815	36.4372	6.8	5.3	355	50	−140
10	06.02.2023	20:37:51.16	37.3030	37.0628	14.5	5.4	182	55	−81
11	06.02.2023	21:15:16.61	38.0708	37.0447	15.9	5.1	50	65	−12
12	06.02.2023	21:57:43.80	38.0568	36.5238	8.6	5.1	15	40	−99
13	07.02.2023	03:08:57.05	37.9615	37.6043	12.1	5.0	197	45	180
14	07.02.2023	03:13:13.34	37.8300	37.6290	25.4	5.6	114	64	−177
15	07.02.2023	07:26:34.70	38.1385	37.6302	15.7	4.5	68	55	45
16	07.02.2023	10:07:17.19	37.3812	37.1273	14.2	3.9	340	78	−175
17	07.02.2023	15:31:28.26	37.3555	37.0788	15.8	5.0	223	34	−11
18	07.02.2023	15:48:52.82	37.9888	36.4592	7.8	5.0	220	51	−85
19	07.02.2023	18:09:58.72	38.1028	36.6345	13.2	5.3	312	86	−152
20	07.02.2023	19:54:21.83	38.6655	39.9365	6.0	4.7	334	84	−159
21	07.02.2023	21:21:25.68	37.9348	37.4097	7.8	4.9	176	51	89
22	07.02.2023	23:13:02.17	36.0775	35.8118	6.9	4.2	206	38	−84
23	08.02.2023	05:52:35.28	38.0635	36.7427	9.1	4.4	204	66	−53
24	08.02.2023	07:48:30.39	38.0297	36.4765	8.8	5.3	249	64	−42

No	Date	Time (GMT)	Lat (°N)	Lon (°E)	H (km)	Mw	Str (°)	Dip (°)	Rake (°)
25	08.02.2023	08:45:33.29	38.1023	37.8105	13.6	4.1	12	42	−95
26	08.02.2023	11:00:17.53	38.1502	37.8267	22.9	4.3	45	80	17
27	08.02.2023	11:11:50.19	38.0180	37.6650	11.4	5.5	106	79	−9
28	08.02.2023	11:23:58.49	37.9917	37.6290	11.7	4.8	96	85	18
29	08.02.2023	14:20:25.75	37.9922	37.3845	7.8	5.0	71	56	−100
30	09.02.2023	07:18:16.42	37.0165	36.6868	16.5	5.0	164	50	−83
31	10.02.2023	01:50:59.13	37.8947	36.6898	7.8	4.4	35	47	−75
32	10.02.2023	04:50:22.38	38.2347	38.1608	11.4	5.0	338	85	171
33	10.02.2023	17:00:49.29	37.9438	36.2668	8.3	5.0	333	79	173
34	11.02.2023	07:55:42.36	37.1235	36.9577	16.5	4.5	178	50	−83
35	11.02.2023	13:09:57.13	38.8490	38.0615	15.4	4.7	132	68	168
36	11.02.2023	14:11:25.29	37.9755	36.3503	8.8	4.1	265	85	−30
37	12.02.2023	16:29:47.51	38.8358	38.0798	15.3	5.2	317	87	169
38	12.02.2023	18:33:14.61	37.3655	36.9433	13.8	4.8	295	83	−173
39	12.02.2023	22:52:58.07	38.0392	36.6095	10.5	4.8	64	11	−43
40	13.02.2023	11:59:16.79	36.9307	36.5358	7.9	4.7	56	49	−45
41	13.02.2023	19:20:26.57	38.0223	36.3910	10.9	4.9	345	67	−149
42	14.02.2023	23:14:01.47	38.5632	37.4538	16.7	4.6	356	74	169
43	15.02.2023	07:36:28.38	38.0285	36.4303	15.4	4.7	350	81	−174
44	15.02.2023	22:25:56.06	38.0637	36.6300	7.8	4.5	225	75	−15
45	16.02.2023	05:18:54.16	38.1358	38.5570	7.3	4.4	357	89	−165
46	16.02.2023	11:16:23.52	35.9620	35.8687	14.8	4.8	210	53	−78
47	16.02.2023	14:45:40.22	38.1872	37.8770	15.4	4.9	331	86	167
48	16.02.2023	19:47:50.07	36.1597	35.8012	17.3	5.0	172	31	−99
49	17.02.2023	00:35:56.31	39.1830	40.2327	17.6	4.9	310	75	−150

No	Date	Time (GMT)	Lat (°N)	Lon (°E)	H (km)	Mw	Str (°)	Dip (°)	Rake (°)
50	17.02.2023	14:58:55.42	37.9338	36.3170	8.7	4.4	203	47	−78
51	17.02.2023	15:34:37.58	38.6607	39.6728	10.7	4.4	10	51	171
52	17.02.2023	19:10:36.09	38.2375	38.2152	13.6	4.1	354	82	−157
53	18.02.2023	05:26:03.41	38.0800	37.1970	12.4	4.1	99	84	−33
54	18.02.2023	19:31:31.19	38.0770	36.6115	8.8	5.3	340	75	−172
55	19.02.2023	00:56:09.67	38.0880	36.2443	6.5	4.6	207	84	147
56	19.02.2023	03:59:10.39	37.2553	36.8310	20.3	4.3	30	48	−70
57	19.02.2023	04:07:40.09	37.2447	36.8550	15.7	4.6	203	46	−104
58	19.02.2023	12:04:32.28	38.2568	38.1992	8.7	4.7	302	72	165
59	19.02.2023	21:30:30.54	37.3798	36.8567	8.1	4.2	209	55	−67
60	20.02.2023	00:37:28.13	38.6488	39.9847	7.2	4.7	51	58	−24
61	20.02.2023	00:39:01.73	38.6433	39.9770	15.7	4.6	343	62	−160
62	20.02.2023	01:07:36.52	38.6797	39.9947	19.9	4.5	72	90	6
63	20.02.2023	01:48:59.08	38.0847	36.8238	11.7	4.7	240	20	49
64	20.02.2023	17:04:29.46	36.1133	36.0820	12.2	6.4	331	80	−124
65	20.02.2023	23:21:15.57	38.0305	37.4375	15.4	4.5	153	44	−81
66	23.02.2023	15:53:46.23	36.1360	36.0530	7.7	5.0	200	37	−97
67	24.02.2023	17:19:50.68	38.8165	37.3843	7.6	4.7	178	80	−169
68	24.02.2023	20:25:31.72	38.1522	38.6985	7.8	4.7	153	83	179
69	27.02.2023	02:51:21.49	37.8942	37.6138	9.4	5.2	183	60	97
70	27.02.2023	06:19:47.18	37.9990	37.0693	14.6	4.4	135	75	131
71	27.02.2023	09:04:50.82	38.2535	38.2932	16.3	5.5	356	81	177
72	28.02.2023	14:39:54.25	37.8335	36.5798	8.0	4.6	19	77	−167
73	28.02.2023	14:49:18.06	37.8487	36.6227	14.0	4.0	40	35	−41
74	28.02.2023	15:16:40.37	38.7205	35.3325	8.8	4.3	135	90	−155

No	Date	Time (GMT)	Lat (°N)	Lon (°E)	H (km)	Mw	Str (°)	Dip (°)	Rake (°)
75	28.02.2023	16:59:12.66	38.7483	35.2907	6.6	4.0	205	85	−18
76	01.03.2023	07:20:23.75	36.3140	36.0557	12.4	4.8	62	50	−97
77	03.03.2023	02:53:43.41	37.8507	36.6463	20.5	5.1	45	38	−106
78	05.03.2023	20:49:45.27	36.7485	36.1270	7.9	4.7	307	68	−173
79	07.03.2023	07:11:16.63	38.4810	37.4532	15.4	5.4	330	84	179
80	07.03.2023	09:40:12.55	37.7203	36.5768	6.7	4.5	293	78	−170
81	07.03.2023	11:47:28.11	38.7098	35.2677	9.7	4.8	325	69	−168
82	07.03.2023	11:53:39.32	38.7078	35.2750	20.4	4.2	324	72	−151
83	07.03.2023	14:18:21.72	38.8102	37.3982	14.0	4.3	15	83	−177
84	09.03.2023	18:55:28.34	38.0592	38.4220	14.3	4.5	351	86	179
85	09.03.2023	23:34:17.42	38.0840	38.4882	7.8	4.0	346	84	−164
86	10.03.2023	02:28:17.60	38.7010	35.2858	6.1	4.8	311	85	−178
87	13.03.2023	01:34:30.22	38.1408	38.6998	12.4	4.8	315	89	−178
88	13.03.2023	02:13:53.39	38.1403	38.6813	8.5	4.5	139	80	158
89	14.03.2023	02:27:52.61	38.1408	38.5297	8.5	3.9	66	80	−28
90	14.03.2023	06:47:36.29	38.0905	36.9432	7.4	4.7	322	84	−178
91	14.03.2023	14:49:48.53	37.8390	37.3933	7.4	4.9	295	75	−3
92	17.03.2023	01:41:14.42	37.9888	36.5313	8.8	3.9	45	70	−3
93	18.03.2023	05:14:29.19	38.0082	36.4525	12.8	4.6	213	43	−81
94	19.03.2023	12:54:26.27	38.0183	36.4855	7.9	4.4	45	20	−92
95	22.03.2023	19:43:25.34	38.1860	38.0590	6.7	4.5	355	40	−164
96	23.03.2023	05:45:22.12	37.8920	36.6120	12.2	4.4	3	58	−103
97	23.03.2023	09:19:53.24	38.0057	36.4477	7.3	5.3	7	66	−145
98	24.03.2023	00:39:53.82	38.0192	36.3958	8.7	4.9	256	50	−38
99	24.03.2023	13:10:35.71	38.0095	37.5475	7.1	4.3	347	87	179

No	Date	Time (GMT)	Lat (°N)	Lon (°E)	H (km)	Mw	Str (°)	Dip (°)	Rake (°)
100	25.03.2023	04:39:32.65	38.0687	37.0170	9.2	4.5	50	50	−7
101	27.03.2023	14:35:16.50	38.0693	36.5107	8.7	4.6	144	80	−159
102	29.03.2023	16:47:01.25	37.9365	36.2922	14.1	4.6	233	59	−41
103	31.03.2023	10:56:58.16	36.9908	36.5998	10.2	4.6	160	70	−1
104	03.04.2023	12:44:15.74	38.0737	37.7003	8.2	4.1	75	77	0
105	07.04.2023	08:29:36.61	39.0335	40.4348	12.4	4.5	317	82	−176
106	19.04.2023	22:44:07.26	38.4465	39.2305	18.9	4.5	335	69	167
107	29.04.2023	01:55:47.44	38.0257	36.4547	17.7	4.9	345	84	163
108	03.05.2023	17:16:38.69	38.0828	36.5757	12.7	5.1	193	56	−105
109	05.05.2023	14:52:31.51	37.9702	36.3023	9.9	4.7	93	73	13
110	08.05.2023	20:20:34.33	38.1178	38.3600	9.0	4.7	333	86	157
111	12.05.2023	08:33:20.41	37.8750	36.2678	11.0	4.6	207	55	−93
112	21.05.2023	12:46:12.76	37.9088	36.2537	14.8	4.8	218	51	−86
113	22.05.2023	16:06:59.17	37.9445	36.2832	15.4	4.7	165	28	−138
114	22.05.2023	16:43:00.23	37.8918	36.2550	14.9	4.3	17	43	−118
115	05.06.2023	16:40:48.26	37.9973	36.5663	15.5	4.5	27	84	−106
116	18.06.2023	15:36:28.31	38.2105	38.5998	9.2	4.5	93	12	−83
117	19.06.2023	18:31:32.47	37.9835	36.5290	15.3	4.7	152	56	−85
118	29.06.2023	05:28:08.81	38.0092	36.4143	11.0	4.2	5	65	−167
119	22.07.2023	10:37:11.13	37.8765	36.2690	17.5	4.0	160	35	−178
120	25.07.2023	05:44:50.06	37.6065	35.9237	13.7	5.6	340	86	173
121	25.07.2023	07:57:56.01	37.5972	35.9365	19.5	4.6	355	60	−167
122	03.08.2023	04:56:18.78	38.2047	38.6565	23.6	4.2	340	51	−176
123	10.08.2023	17:48:01.63	38.2865	38.2120	21.6	5.2	339	67	−142
124	12.08.2023	13:39:16.24	38.3075	38.2352	23.4	4.9	342	83	−159

No	Date	Time (GMT)	Lat (°N)	Lon (°E)	H (km)	Mw	Str (°)	Dip (°)	Rake (°)
125	16.08.2023	14:36:59.48	37.6585	35.3950	24.7	4.6	194	51	−124
126	22.08.2023	10:17:34.55	38.4373	36.6917	14.8	4.8	273	76	140
127	24.08.2023	05:35:24.12	38.2652	38.2040	11.7	5.0	343	79	−171
128	09.10.2023	06:28:55.39	38.2409	38.2201	11.3	3.9	155	70	164
129	09.11.2023	02:32:13.09	36.6203	36.3702	14.4	4.6	198	54	−51
130	15.11.2023	22:32:10.59	38.1882	38.5399	12.9	4.0	218	80	−18
131	20.11.2023	07:36:05.28	38.2304	38.7605	10.7	4.5	315	74	177
132	23.11.2023	14:46:08.17	38.1422	38.5635	13.6	5.2	141	75	−171
133	21.12.2023	18:24:33.48	36.3308	36.1531	8.7	4.1	223	60	−25
134	28.12.2023	09:34:05.32	38.2664	38.1217	18.4	4.6	240	86	−32
135	30.12.2023	13:26:24.18	38.4564	39.0192	9.5	4.2	238	45	15
136	08.01.2024	13:19:12.62	38.2842	38.7525	12.7	4.4	334	86	−155
137	09.01.2024	19:20:09.08	38.0058	37.4911	8.3	4.1	45	69	−155
138	10.01.2024	19:38:43.27	36.1811	35.9250	11.5	4.2	190	41	−45
139	18.01.2024	20:37:23.14	38.1194	38.4336	9.7	4.0	242	66	25
140	19.01.2024	22:27.34.63	38.8275	37.4694	6.8	4.4	179	87	−168
141	21.01.2024	12:41:35.28	38.3686	38.8425	12.4	4.0	145	61	135
142	25.01.2024	13:04:06.82	38.1989	38.4589	10.6	5.2	145	74	−164
143	25.01.2024	22:01:49.05	37.8542	36.1428	13.5	4.4	12	66	−105
144	16.02.2024	03:54:07.21	38.2728	37.8003	9.2	4.1	187	24	−110
145	19.02.2024	09:23:21.54	38.0933	37.8128	18.2	4.3	260	78	45
146	01.03.2024	14:09:54.34	37.2908	37.1389	7.8	4.1	202	77	19
147	03.03.2024	14:43:55.42	38.0608	37.6497	12.7	4.4	339	53	−153
148	20.03.2024	05:55:42.29	37.4856	36.9886	8.4	4.0	350	81	−167
149	25.03.2024	10:10:46.44	37.8519	36.2506	12.3	4.0	245	75	−61

No	Date	Time (GMT)	Lat (°N)	Lon (°E)	H (km)	Mw	Str (°)	Dip (°)	Rake (°)
150	30.03.2024	00:25:04.57	38.5044	39.3592	13.8	4.7	243	85	8
151	03.04.2024	07:48:14.51	38.0394	37.6789	14.2	4.5	270	90	−20
152	12.04.2024	05:44:27.16	38.2361	38.5719	11.4	4.1	240	38	15
153	16.04.2024	21:09:49.43	38.1472	38.5606	9.6	4.3	245	80	−10
154	02.05.2024	20:57:28.19	38.4617	39.2306	8.9	4.0	235	60	30
155	20.05.2024	12:28:21.48	38.4608	39.2592	13.7	4.0	210	85	35
156	05.06.2024	07:37:50.64	36.1683	35.9289	9.7	4.1	200	55	−35
157	06.06.2024	10:47:49.18	38.0883	38.3358	11.5	4.2	235	75	−12
158	09.06.2024	03.31:57.09	37.9987	36.4058	10.7	4.3	75	90	25
159	16.06.2024	17:24:51.68	38.2667	37.8097	13.9	4.4	65	42	−90
160	26.06.2024	04:42:50.17	39.2428	40.8936	11.7	4.0	40	85	15
161	09.07.2024	21:41:03.62	38.2422	38.1206	8.6	4.2	250	90	20
162	10.07.2024	09:54:31.11	38.2581	38.1208	14.3	4.3	255	80	25
163	26.07.2024	15:27:17.32	39.2736	40.9750	11.9	4.2	280	85	−155
164	01.08.2024	02:52:12.59	38.1569	38.2889	15.2	4.4	245	85	−175
165	07.08.2024	02:32:27.75	37.6417	35.8789	9.4	4.6	70	90	−10
166	07.08.2024	02:33:12.25	37.6628	35.8681	10.2	4.5	250	85	15
167	07.08.2024	02:34:25.38	37.6553	35.8761	8.6	4.0	85	90	−15
168	19.08.2024	09:02:58.31	38.2806	37.7494	10.3	4.0	135	50	−135
169	20.08.2024	00:57:42.10	36.4905	36.4726	13.8	3.7	97	67	−39
170	23.08.2024	11:59:45.22	37.8625	36.2878	14.9	4.0	351	59	−159
171	07.09.2024	06:31:10.19	37.2842	37.0447	14.2	5.0	215	60	−20
172	17.09.2024	22:38:40.75	38.2169	38.6217	12.4	4.4	247	45	−7
173	16.10.2024	07:46:32.82	38.3658	38.7961	15.2	5.9	343	75	−154
174	19.10.2024	11:41:09.39	37.6006	37.1681	11.5	4.4	259	55	−61

No	Date	Time (GMT)	Lat (°N)	Lon (°E)	H (km)	Mw	Str (°)	Dip (°)	Rake (°)
175	27.10.2024	17.07:09.16	37.6497	35.9358	9.8	5.0	75	87	−25
176	03.11.2024	22:58:30.62	38.1522	38.5850	12.5	4.2	255	81	18
177	15.11.2024	07:46:20.18	38.0036	37.5914	13.3	4.9	130	75	5
178	25.11.2024	17:20:04.54	38.1622	37.8550	10.7	4.6	300	88	176

4. Coulomb stress change

The static Coulomb stress change caused by a mainshock has been widely applied to assess areas of subsequent off-fault aftershocks (Reasenberg and Simpson, 1992; Toda et al., 2008; 2011a). The Coulomb stress change is defined as $\Delta CFF = \Delta\tau + \mu\Delta\sigma$, where τ is the shear stress on the fault (positive in the inferred direction of slip), σ is the normal stress (positive for fault-normal tension) and μ is the apparent friction coefficient. Failure is promoted if ΔCFF is positive and inhibited if negative; both increased shear and unclamping of faults are taken to promote failure, with the influence of unclamping controlled by fault friction (Toda et al., 2011a). After the occurrence of an earthquake, the areas with positive values of ΔCFF are loaded with stress. To resolve the Coulomb stress change on a 'receiver fault' requires a source model of the earthquake fault slip, as well as the geometry and slip direction on the receiver (Toda et al., 2011a). At each point of Coulomb stress increase, we can identify the receiver faults that maximize both the earthquake-induced stress change and the tectonic stress (King et al., 1994), termed the "optimally oriented" Coulomb stress change (Toda et al., 2011a). Toda et al. (2011b) published the MATLAB code for Coulomb stress distribution that can be downloaded on the web page (https://pubs.usgs.gov/of/2011/1060).

5. Results

5.1 The 6 February 2023 Pazarcık-Elbistan Source Mechanisms

In this section, we present a total of 178 centroid moment tensor (CMT) solutions of events with ($Mw \geq 3.7$) occurred along the EAFZ and surrounding area in the period between 3 February 2023 and 25 November 2024. The results of the moment tensor solution for the 178 selected events are given in Table 2. From the spatial distribution of the CMT solutions (Figs. 4 and 5), we observe a prominent NE-SW alignment of nodal planes. The along-strike length of the activated zone is ~400 km, and the analyzed events mostly align along the EAFZ and its western branch formed by the Sürgü (SüF), Çardak (ÇF) and Savrun (SaF) faults. The moment magnitudes (Mw) range from 3.7 to 7.7. Figure 4 and Fig. 5 display in map view the 178 fault plane solutions in lower-hemisphere projection. Predominant activity is observed throughout the EAFZ in a cluster-type distribution. The average strike and dip angles along the Çardak Fault (ÇF) that we found are N359° and 79° to the NE, respectively. The two mainshocks have similar focal mechanism indicating left-lateral slip on steep north-west and north dipping, NE-SW and EW trending planes along the EAFZ and ÇF, respectively, in very good agreement with the tectonic and structural characteristics of the area. In the following sections, for further analysis, we focus on the orientations of the axes of maximum compression (P) and tension (T). To analyze the data set for spatial clustering of similar faulting mechanisms we proceed as follows: first, the Pazarcık-Elbistan EQ region is divided into six clusters comprising the 178 events (see Fig. 6; Table 3). This subdivision is based on structural and geological information on fault segments, as well as on spatial clustering of hypocenters, which define a steep NE-SW trending plane of activity along the EAFZ and a diffuse cluster like type of activity in the Pazarcık-Elbistan region. Note that this difference in hypocentral distribution is real and not an artifact of varying location precision (horizontal and vertical errors <2 km) within the area (Fig. 6).

The Çardak Cluster (ÇC) contains 52 fault plane solutions at depths between 4 and 21 km and with a moment magnitude (Mw) range between 3.9 and 7.6. ÇC includes the Elbistan mainshock and the aftershocks occurred on the

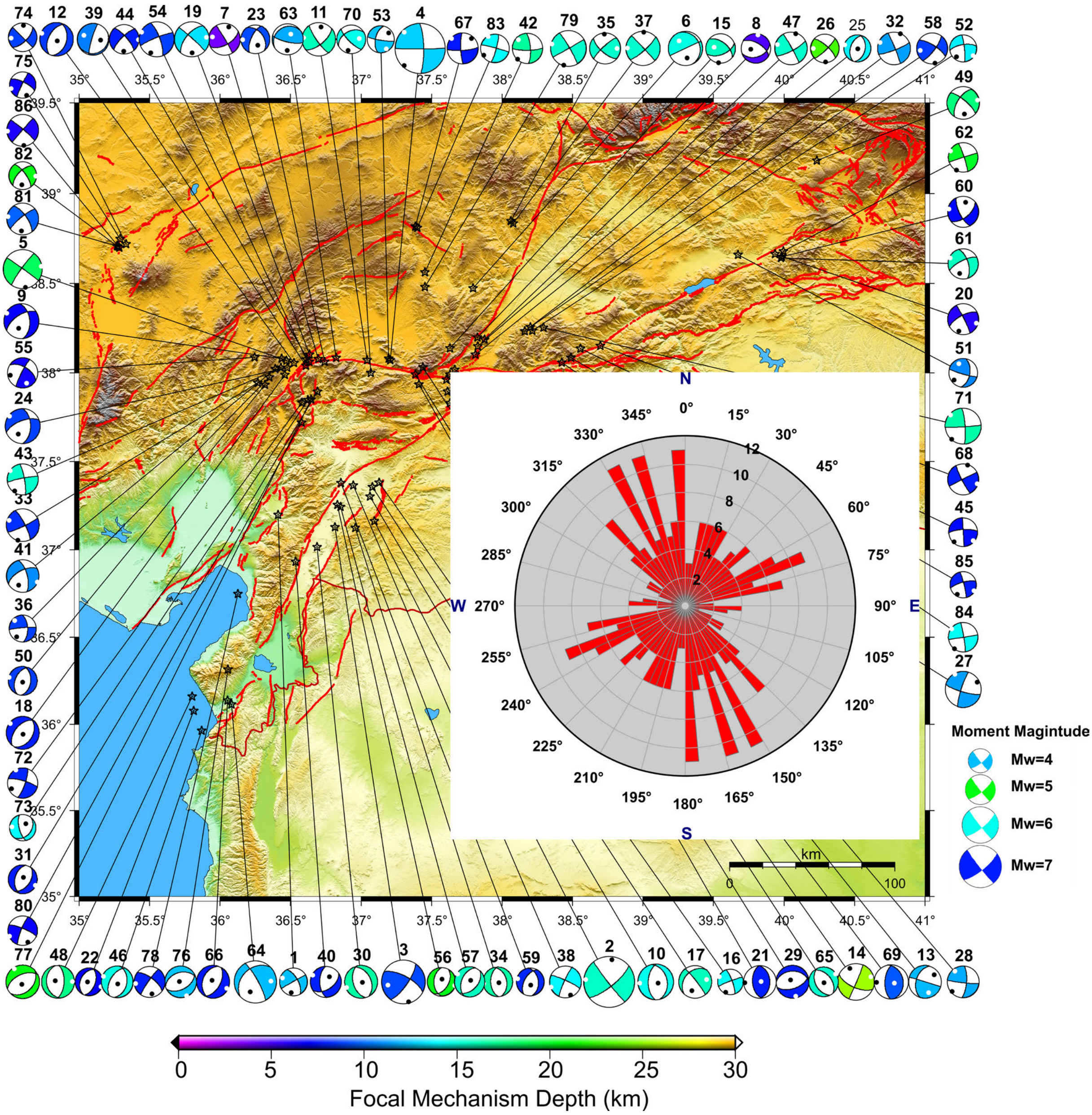

Figure 4. Topographic map showing CMT solutions obtained using the waveform inversion method of Nakano et al. (2008). Focal mechanisms are projected onto the lower hemisphere and scaled by magnitude. The CMT dataset spans the period from 3 February 2023 to 25 November 2024. Black and white circles on the beach balls represent the P- and T-axes, respectively. Beach-ball colors correspond to the source depth distribution of the focal mechanisms (see the colored bars for depth reference). The rose diagram in the map shows orientations of the entire focal mechanism catalogue.

Çardak and Savrun faults. The average faulting mechanisms within ÇC reflect predominantly NNE-SSW-extensional, left-lateral strike-slip faulting, with some solutions indicating normal faulting (Figs. 4 and 5). The Doğanşehir Cluster (DC) covers the area surrounding the Malatya province and contains 26 events. These events occurred at depths between 5 and 25 km. Their spatial distribution reflects the down-dip extension of the surface trace of the Elbistan rupture. Event magnitudes range from 4.0 to 5.6. The distribution of P and T axes indicates predominantly strike-slip faulting with a normal component (Figs. 4 and 5). The P axes reflect a scattered orientation with an average NNE-SSW trend and the T axes are found to cluster at a sub-horizontal ESE-WNW trend (Fig. 7). East of the Doğanşehir Fault, there are 34 fault plane solutions. We subdivided these 34 source mechanisms according to the spatial aftershock distribution and created the two Sürgü (SC, 11 events) and Erkenek (EC, 23 events) clusters (Figs. 6 and 7).

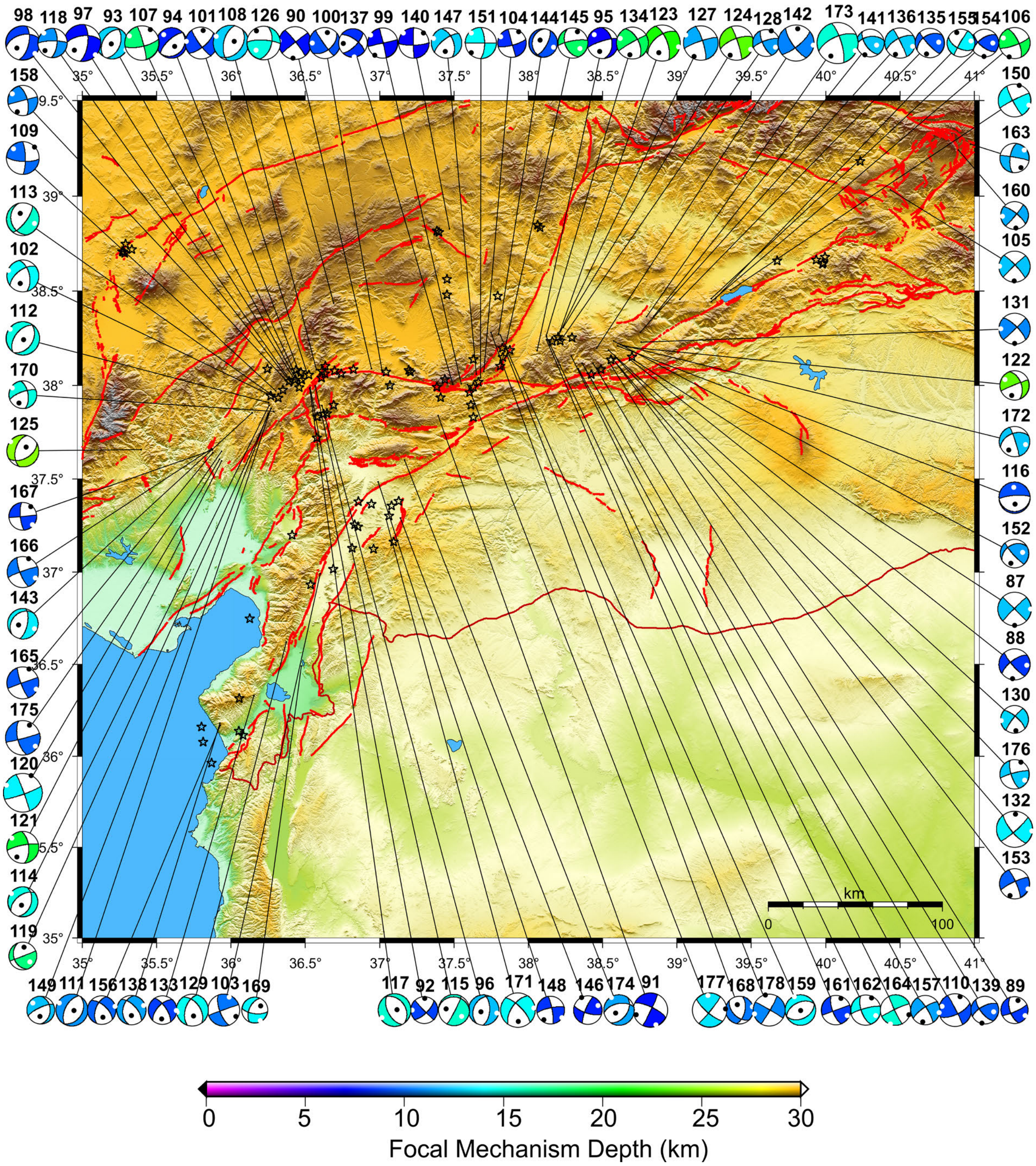

Figure 5. Topographic map showing CMT solutions obtained using the waveform inversion method of Nakano et al. (2008). Focal mechanisms are projected onto the lower hemisphere and scaled by magnitude. The CMT dataset spans the period from 3 February 2023 to 25 November 2024. Same as Fig. 4.

These clusters have clear NE-SW P-axis and NW-SE T-axis orientations. The southern zone of EAFZ is divided into Pazarcık (PC) and Amanos (AC) clusters, which consist of 13 and 11 aftershock faulting mechanism solutions, respectively. The P axes are trending NNE-SSW at various dip angles and the T axes are trending E-W at shallow dip angles. Therefore, this area reflects both strike-slip and normal faulting mechanisms (Fig. 7).

Figure 8 exhibits 178 aftershock focal mechanisms in ternary (triangular) diagram (Frohlich, 1992). The solutions are color-coded according to faulting type following the classification of Frohlich (1992) based on P and T-axis plunge angles. Frohlich (1992) categorized focal mechanisms as strike-slip, reverse, normal and "odd" events. Very few reverse faulting events occur among the analyzed aftershocks. The strike-slip aftershocks (red beach-balls in Fig. 8) are distributed across the Çardak, Doğanşehir, Sürgü, Erkenek and Pazarcık clusters, whereas normal faulting events (green

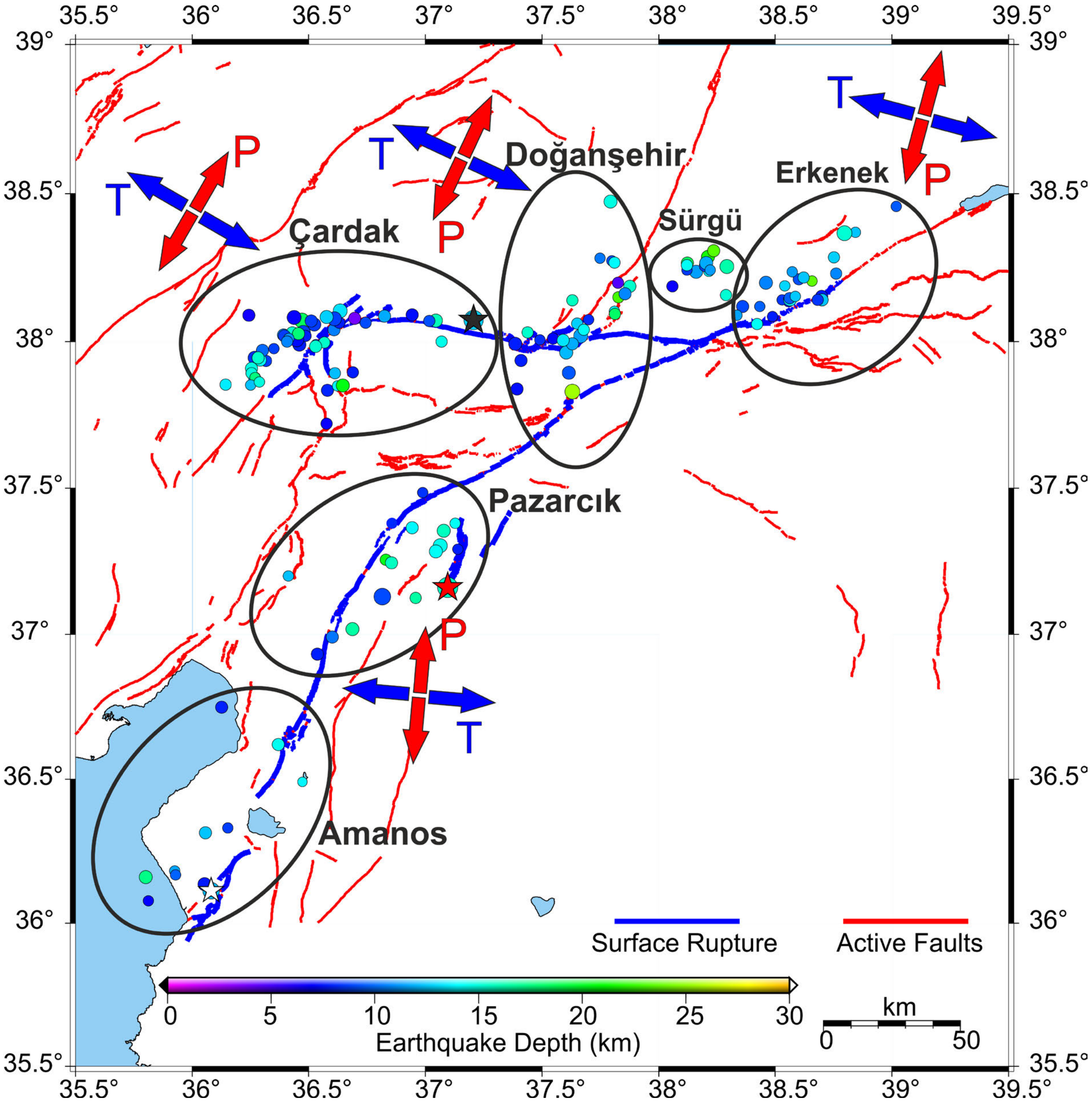

Figure 6. Epicenter distribution map of the focal mechanism solutions (Mw ≥ 3.7) in the Pazarcık-Elbistan EQ area. The size of circles in the map scales with magnitude and the coloring indicates the hypocentral depth (lighter color = shallower depths). Blue lines represent the total Pazarcık-Elbistan EQ rupture from aftershock spatial distribution. Ellipses exhibit each cluster location.

beach-balls in Fig. 8) occur mainly in the Çardak, Doğanşehir, Pazarcık, and Amanos clusters. Aftershocks of the "odd" type (gray beach-balls in Fig. 8) correspond to oblique faulting, combining strike-slip and normal mechanism (see the ternary diagram in Fig. 8). These oblique events are observed mostly in Çardak, Doğanşehir and Amanos clusters.

5.2 Analysis of stress tensors

To determine the stress field orientation in the Pazarcık-Elbistan earthquake region along the EAFZ from fault mechanism data, we first inverted the complete dataset of 178 fault plane solutions to estimate the stress tensor. In a second step, we performed independent inversions for each cluster to identify variations local stress field orientation, relative stress magnitude, and shape ratio (Figs. 9 and 10). We carried out separate inversions for each cluster to account for the fault segmentation and to reduce the effects of fault geometric heterogeneities. According

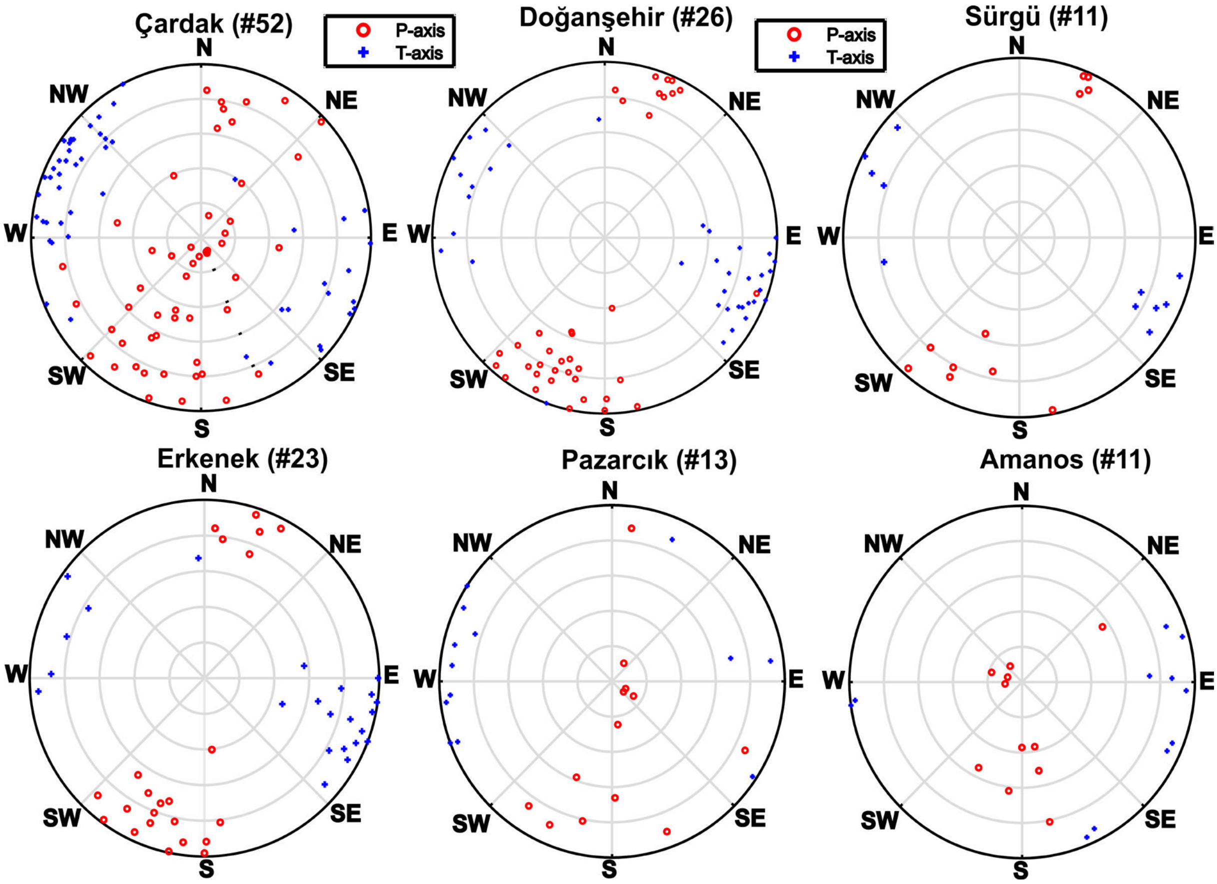

Figure 7. Distribution of P and T axes for the different clusters (i.e., Çardak, Doğanşehir, Sürgü, Erkenek, Pazarcık and Amanos) in equal-area lower hemisphere projection.

to the analysis performed using the approach proposed by Vavryčuk (2014), the stress field in the Pazarcık-Elbistan earthquake region exhibits some degree of heterogeneity; however, the inversion results remain within acceptable limits. In particular, β values $\leq 33°$ – together with low misfits (<0.4) for strike, dip, and rake – indicate that the stress tensor solutions are reliable (Fig. 9). Thus, the level of heterogeneity inferred from the average β values is moderate and does not compromise the overall interpretation of the stress field. For each stress inversion, 2000 bootstrap iterations were performed. In order to further resolve the source of stress field heterogeneity, subsets of the fault plane data are formed based on the inferred extent of the ruptures of the two mainshocks, structural variations within the area of investigation and aftershock hypocenter distribution as discussed in the previous section. Results of the individual inversions are given in Table 3. Inverting the subsets for the ÇC and the DC result in a significantly low β value of 18° for ÇC and 21° for DC (Fig. 9). Also, the β of SC and EC that yields <20° are remarkably low. Inversion of the SC and EC subsets indicate that both segments separately exhibit a relatively low level stress heterogeneity, with β = 15° and β = 11°, respectively. Finally, we inverted the two southern clusters, PC and AC, to determine the stress fields acting on the Pazarcık, Amanos and Narlı faults. Both PC and AC yield relatively low β (misfit angle) values of 21° and 20°, respectively.

A clear NW-SE transcurrent regime (strike-slip faulting regime) is found for the ÇC area with an almost horizontal orientation for $\sigma 3$ (plunge 5°) (Fig. 9, Table 3). The relative stress magnitude or shape ratio for the ÇC area is 0.17 indicating the existence of a transpressional stress regime. Similarly, a strike-slip regime with a notable normal faulting component is observed in the DC area ($\sigma 1$ trend N218°E, plunge 35°; $\sigma 2$ trend N39°E, plunge 55°) (Figs. 9 and 10, Table 3). The shape ratio is estimated at 0.45 for the DC area (Doğanşehir Fault). The confidence intervals of $\sigma 1$ and $\sigma 2$ strike in NE-SW direction largely overlap. A shape ratio of 0.66 in the SC indicate a NW-SE transtensional strike-slip faulting regime near the Sürgü Fault (Fig. 10). Similarly, the EC shows a strike-slip stress regime with a normal component; $\sigma 1$ is sub-horizontal trending N195°E with a plunge of 14°, and a shape ratio of 0.61 (Figs. 9 and 10; Table 3). The stress field at the Pazarcık Fault is similar to that identified at the

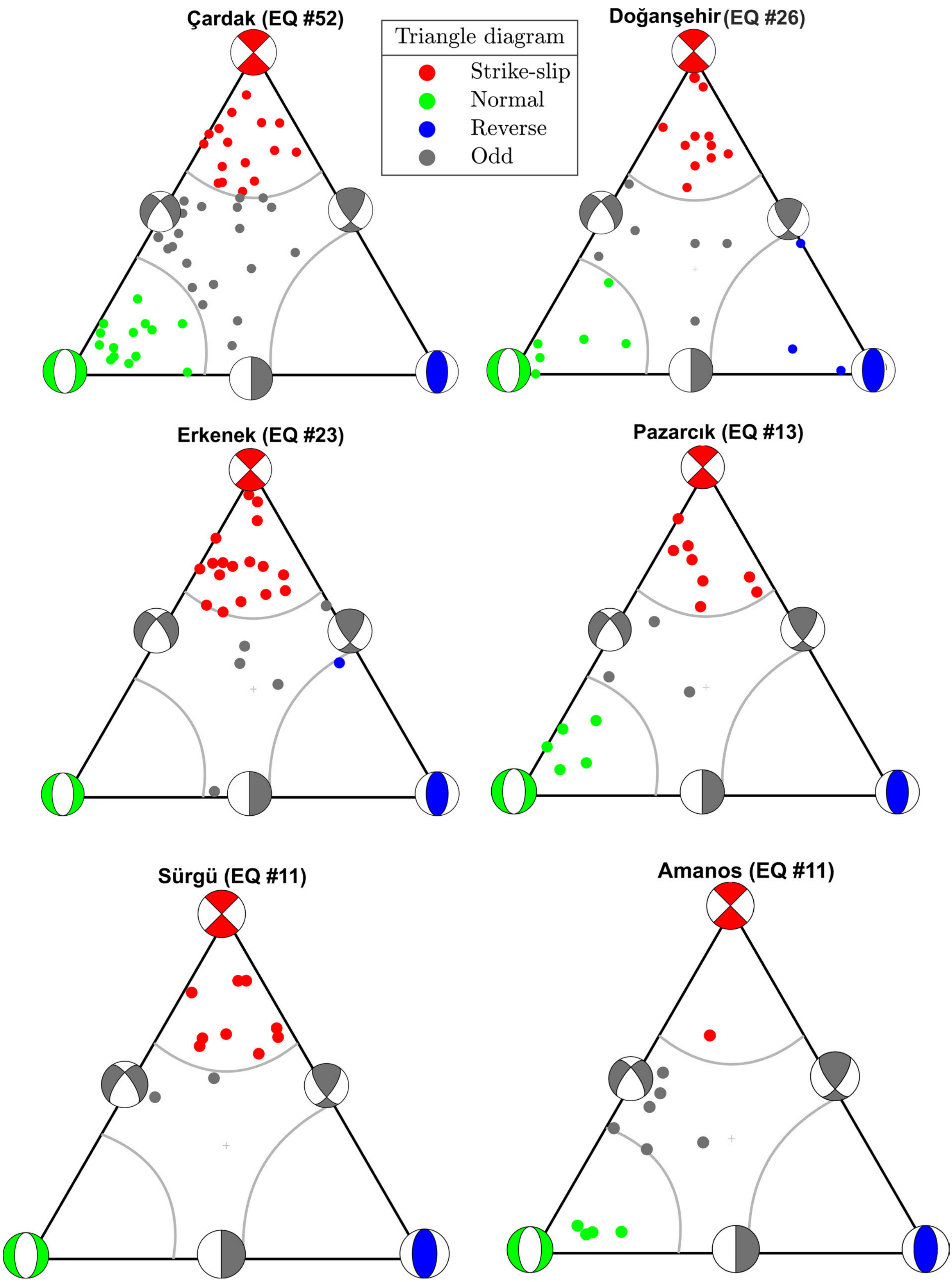

Figure 8. The triangle diagram (Frohlich, 1992) for displaying the distribution of the 178 focal mechanism solutions in the six analyzed clusters.

Amanos Fault but with a $\sigma1$ rotated by ~37° counterclockwise and plunges of 54° and 73°, respectively. The Pazarcık Fault may represent the main active branch of the EAFZ, bounded to the south by the NNE-SSW trending Amanos

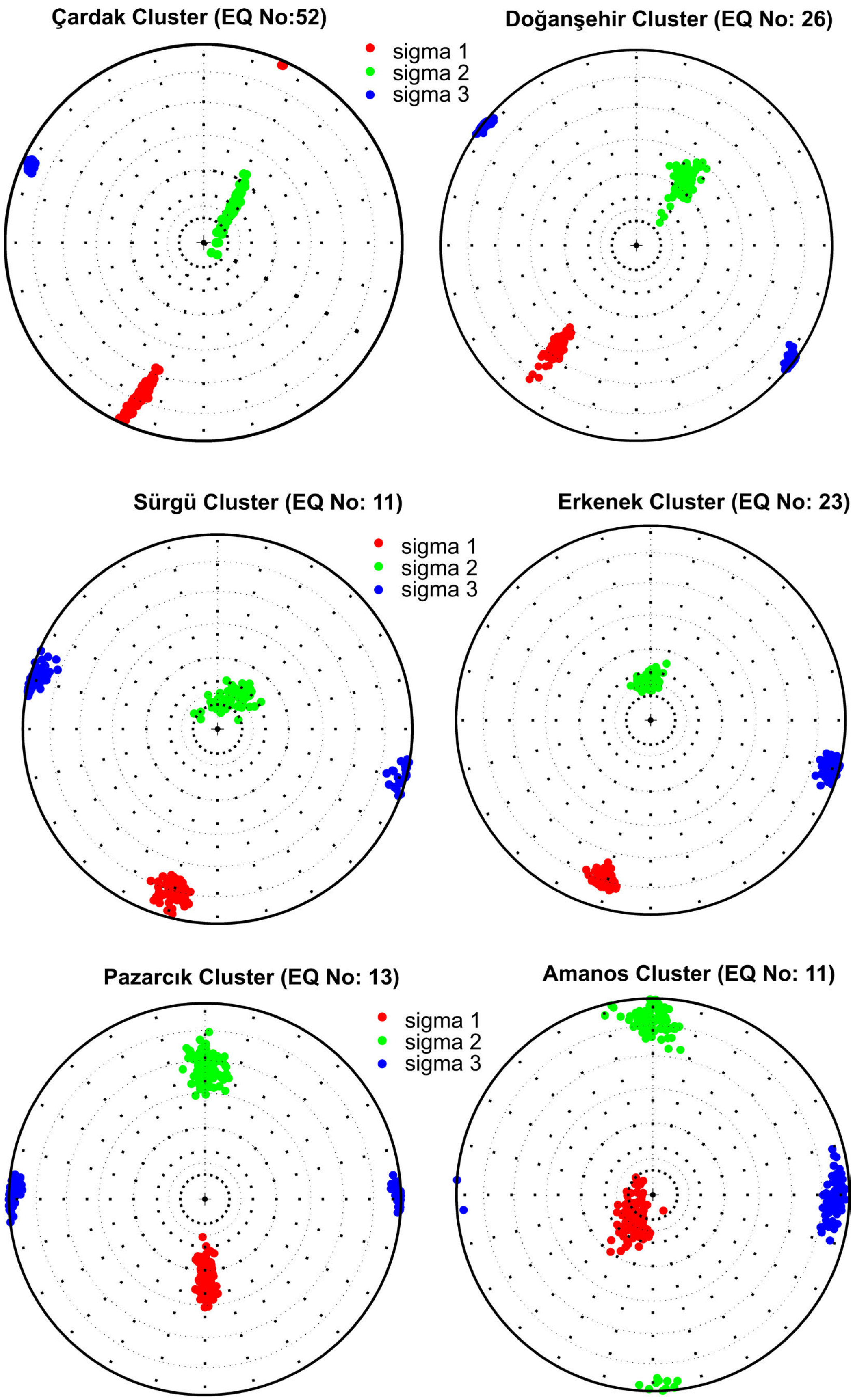

Figure 9. Confidence limits of the principal stress directions retrieved by the iterative method (Vavryčuk, 2014) for each cluster along the Pazarcık-Elbistan earthquake region. Red, green and blue colors correspond to the $\sigma 1$, $\sigma 2$ and $\sigma 3$ stress directions, respectively. The contours around the best model define the 95% confidence region of each stress axis (upper side).

Fault (Figs. 4, 5, 6 and 7). The resulting stress tensors are complex and corresponds to both transpressional ($R < 0.5$) and transtensional stress regimes ($R > 0.5$). In summary, the orientation of the maximum horizontal compressional stress (SH) is predominantly NE-SW and a strike-slip stress regime with a moderate normal faulting component is found across all clusters. Moreover, an N-S orientation of SH and a dominant extensional stress regime are observed in the Pazarcık and Amanos Clusters (Fig. 9, Table 3). Inspection of Figs. 9 and 10 shows that it is clear that the ÇC, DC, SC and EC areas share a very similar stress regime within the uncertainties of the results (see the red, blue and green dots in Fig. 9). Although these clusters exhibit broadly similar stress regimes, minor differences are observed in the orientations and magnitudes of the principle stresses. After clustering these areas, the overall similarity in stress regimes becomes more apparent, with only small variations among these fields. In contrast, the PC and AC clusters exhibit an unusual pattern, with near vertical $\sigma 1$ axes, indicating an extensional regime. This observation is inconsistent with their location along the EAFZ, which represents the principal transcurrent shear zone. The AC area, in particular, reflects a complex interaction of major faults systems separated by local basins and trenches interconnected by secondary fault segments. Given the similar $\sigma 1$ orientations and focal mechanisms, we interpret the faults in this cluster as representing a transition zone between the Dead Sea Fault (DSF) and the EAFZ. The AC area likely corresponds to a pull-apart structure developed through transtensional interaction between the Amanos Fault and the northern segments of the DSF (Ergin et al., 2004).

To investigate spatial variations of the stress field across the entire data set (178 fault plane solutions) we applied the relevant modules of the ZMAP software package (Wiemer, 2001). The inversion algorithm of Vavryčuk (2014) was used to quantify stress heterogeneity and β along the Pazarcık-Elbistan earthquake region. High variance, or high β, indicates a poor fit of a homogeneous stress tensor to the observed focal mechanisms, and reflects a high degree of stress field heterogeneity (Michael et al., 1990; Lu et al., 1997; Wiemer et al., 2002; Görgün et al., 2010). The results of the stress tensor inversions based on subvolumes with a horizontal radius of 1 km, no depth limitation and containing at least 12 focal mechanisms are shown in map view in Fig. 11a. The orientation of the maximum principal stress ($\sigma 1$) derived from the inversion is plotted across the Pazarcık-Elbistan region of the EAFZ (Fig. 11a). The observed variations in orientations reflect the heterogeneity of the stress field which influences both the principal stress directions and the faulting styles across the study area. This behavior is consistent with the local stress fields described above. Notably, the Çardak Fault was active after the Pazarcık event and prior to the Elbistan event only in its western segment, near the bending point of the EAFZ (i.e., at the intersection of the Çardak, Sürgü and Pazarcık faults) (Fig. 11a). The northern segment of the Çardak Fault, north of the Pazarcık Fault, was activated only during the Pazarcık mainshock and is therefore sampled primarily by the Pazarcık aftershocks used in this study. The variance of the resulting stress tensors for each subvolume is calculated and shown as a color-coded map in Fig. 11b. Relatively low stress variance (0.15) is observed across most of the Pazarcık-Elbistan region, whereas higher values (>0.2) are concentrated in the Elbistan area, particularly along the Çardak, Sürgü and Erkenek faults. According to Wiemer et al. (2002), a low degree of stress heterogeneity (variance < 0.2) indicates a relatively uniform stress field. Therefore, to first order, the Pazarcık-Elbistan region is characterized by a homogeneous intraplate stress field in terms of event clustering.

Stress tensor inversions of the aftershock focal mechanisms show rotations of the local stresses following the Pazarcık and Elbistan mainshocks. In the Pazarcık-Elbistan mainshock area, the maximum horizontal compressive stress axis is horizontally rotated clockwise by ~65° with respect to the coseismic and long-term regional stress field. Towards the northern end of the rupture (north of the Elbistan mainshock area), stresses are rotated clockwise steadily. We conclude that the Pazarcık earthquake caused significant stress partitioning along the rupture. The direction of stress rotation is related to the orientation of the individual fault segments as the Çardak Fault along the EAFZ (Fig. 11a).

As we observe a marked decrease in stress variance and β values (misfit angle) over time in the fault plane solution catalogue, it is necessary to assess whether this observation has a physical basis. To this end, we performed tests using randomly defined subsets of the catalogue, in which both the number of input data and the regional-scale spatial distribution of events are comparable to those used in the scale-dependent analysis (e.g., 50 fault planes with a step size of 10). Stress tensor inversion results from these randomly generated subsets show that stress variance and β values decrease prior to June 2023 and increase again thereafter. The temporal evolution of stress variance and β does not depend on the number of input data (Fig. 12), as confirmed by tests using different input sizes and step lengths. The observed decrease and subsequent increase in stress variance and β values may reflect changes in stress-field orientations and heterogeneity associated with the temporal evolution of aftershock distributions.

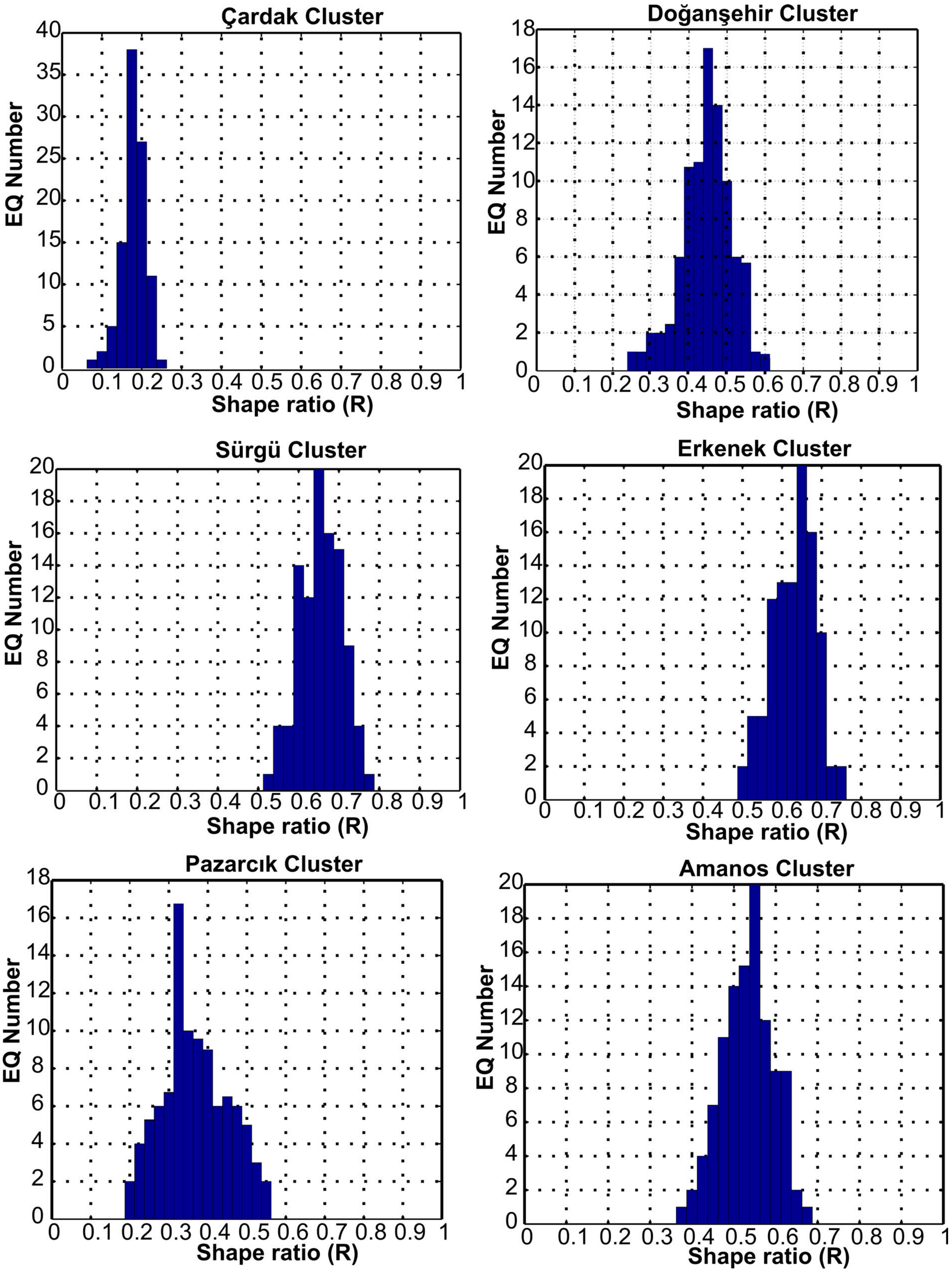

Figure 10. Histograms of the stress/shape ratio (R) are shown in the bottom side for each cluster. These values indicate that the Çardak, Doğanşehir and Pazarcık show a transpressional stress regime (R < 0.5) while Sürgü, Erkenek and Amanos are described by transtensional stress regime (R > 0.5).

Table 3. Results of stress tensor inversion for the six clusters comprising a total of 178 focal mechanisms in the Pazarcık-Elbistan earthquake region. Note: The results include the number of fault plane solutions within each cluster, the orientation of the three principal stresses (σ1-σ3) expressed as trend and plunge, the average misfit angle (β), and the stress (shape) ratio (R).

Cluster Name	EQ Number	σ1 (trend/plunge)	σ2 (trend/plunge)	σ3 (trend/plunge)	R (shape ratio)	σ1 (misfit)	σ2 (misfit)	σ3 (misfit)
Çardak	52	203°/15°	43°/75°	294°/5°	0.17	18°	18°	3°
Doğanşehir	26	218°/35°	39°/55°	308°/0.5°	0.45	21°	21°	10°
Sürgü	11	193°/18°	34°/71°	285°/6°	0.66	15°	22°	17°
Erkenek	23	195°/14°	341°/73°	102°/9°	0.61	11°	14°	10°
Pazarcık	13	181°/54°	357°/36°	89°/2°	0.31	21°	21°	11°
Amanos	11	218°/73°	352°/12°	85°/12°	0.57	20°	22°	20°

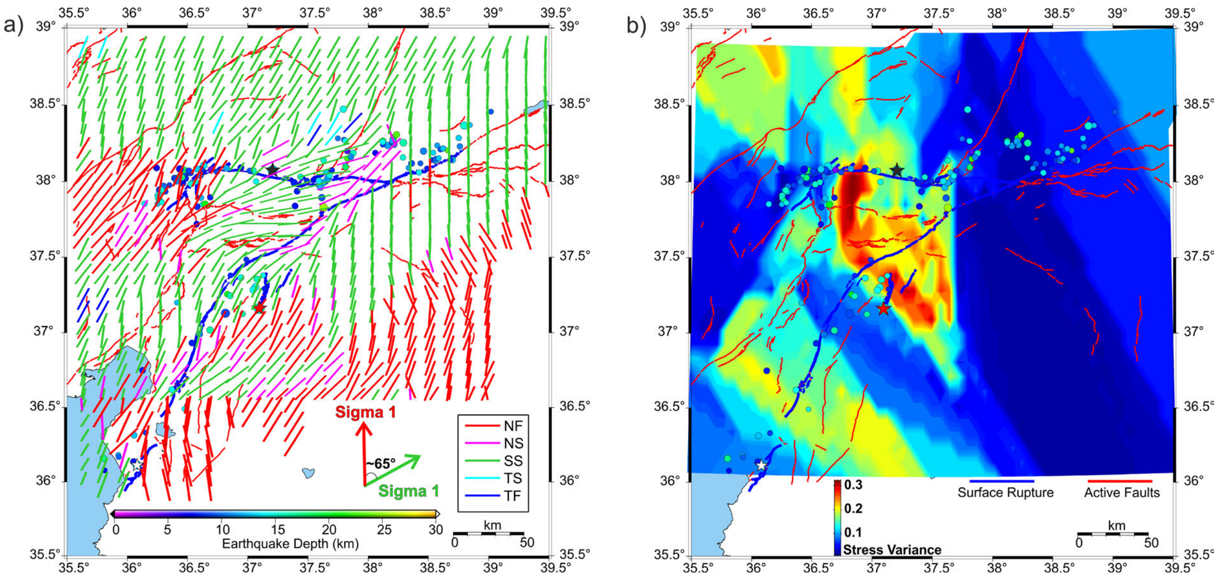

Figure 11. (a) Orientation of the σ1 trend (bars) within gridded subvolumes (1 km^2 with no depth limitation), smoothed over a 1 km radius at each grid node. Faulting regimes are indicated by colors as shown in the legend. The following abbreviations describe the tectonic stress regime (Zoback, 1992): NF = Normal faulting, NS = Predominately normal faulting with a strike-slip component, SS = Strike-Slip faulting, TS = Predominately thrust faulting with a strike-slip component, TF = Thrust faulting. Black and red stars denote the epicenters of the Mw7.6 Elbistan and Mw7.7 Pazarcık mainshocks, respectively. b) Spatial distribution of the stress tensor variance at each node corresponding to (a), following Vavryčuk (2014). High variance (>0.2) indicates strong stress field heterogeneity.

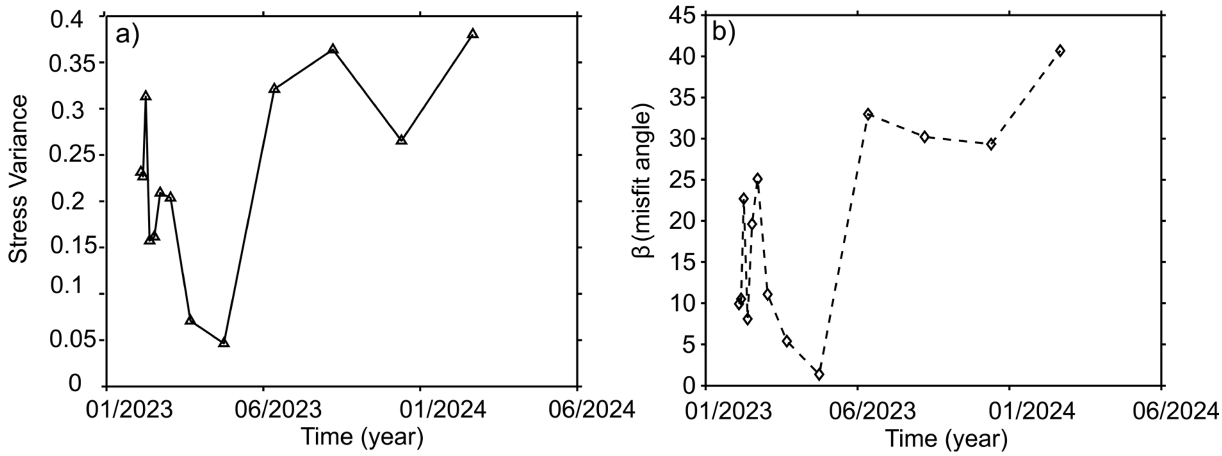

Figure 12. Stress tensor inversion results plotted as a function of time. a) Stress variance and b) β (misfit) values vs. time, respectively.

5.3 Calculation of the Coulomb stress change

The source parameters derived from waveform modelling were used to calculate Coulomb stress changes for the three largest events (Table 2). The principal axes of the stress tensor ($\sigma1$, $\sigma2$ and $\sigma3$) were also incorporated to compute the spatial distribution of Coulomb stress changes (Fig. 13). Stress changes were resolved at depth of 10 km based on the estimated geometry of the major active faults. Increases in shear stress in the rake direction, together with fault unclamping, are interpreted to promote failure on surrounding "receiver" faults (Toda et al., 2008). We resolved the shear and normal (clamping/unclamping) components of the stress change on a 2D grid of points and on specified "receiver" fault planes. A regular grid of receiver faults was constructed with a spacing of 5 km. Receiver faults are planes with specified strike, dip, and rake on which stresses imparted by the source faults are resolved; these are referred to as 'specified faults" in the Coulomb stress calculation. Changes in shear stress depend on the position, geometry, and slip of the source fault, as well as on the position and geometry of the receiver fault, including its rake. In contrast, the normal stress changes (clamping or unclamping) are independent of the receiver fault rake (Toda et al., 2011b). The Coulomb 3.3 software (www.coulombstress.org) was used to model the Pazarcık-Elbistan mainshocks as strike-slip sources at depths of 16-13 km, with a strike/dip/rake of 142°/86°/−165° and 359°/79°/178°, respectively, assuming a friction coefficient $\mu = 0.4$ in an elastic half space with uniform isotropic elastic properties (Lin and Stein, 2004; Toda et al., 2005; 2008; 2011a). In addition, we analyzed the Mw6.4 Samandağ earthquake, which occurred in Hatay Province at 17:04 GMT on 20 February 2023. This event is characterized by normal faulting with a strike/dip/rake of 331°/80°/−124°.

The spatial distributions of Coulomb stress changes associated with the 2023 Pazarcık-Elbistan earthquake sequence is shown in Fig. 13. We analyzed the three mainshocks (as described in the preceding section) with Mw larger than 6.0. Our results indicate that these events produce similar Coulomb stress transfer patterns across the Pazarcık-Elbistan region. The red lobes in Fig. 13 represent areas of increased Coulomb stress, where faults can be brought closer to failure. For Pazarcık Mw7.7 mainshock, positive Coulomb stress changes are observed predominantly in NNE-SSW direction along the rupture zone (Fig. 13a). The Elbistan Mw7.6 mainshock exhibits Coulomb stress increases primarily in the E-W and N-S directions (Fig. 13b). The Samandağ Mw6.4 aftershock event shows a similar NNE-SSW-oriented stress distribution (Fig. 13c). The NE and SW ends of the Pazarcık-Elbistan rupture zone are brought approximately 3-5 bars closer to failure. Stress changes ≥ 1 bar are generally considered sufficient to influence seismicity rates (King et al., 1994). Prior to the Elbistan Mw7.6 mainshock, a significant stress increase of up to ~5 bars is observed along the Çardak Fault, where the Elbistan event subsequently occurred (Fig. 13a). This suggests that the Elbistan earthquake was likely triggered by the Pazarcık event. Although both events exhibit similar focal mechanisms, their fault strike differ. The Mw6.4 Samandağ event, the largest aftershock of the Pazarcık-Elbistan earthquake sequence, occurred approximately two weeks after the Mw > 7.5 mainshocks of 6 February 2023. This event is important for Coulomb stress evolution, as it appears to contribute to the southeastward migration of seismicity, consistent with the regional stress field of the Pazarcık-Elbistan sequence.

To further compare the Coulomb stress changes with aftershock distribution, three cross-sections are presented in Fig. 14 along profiles A-A′ (Pazarcık), B-B′-(Elbistan) and C-C′ (Samandağ), oriented perpendicular to the fault geometry. Most aftershocks (Mw ≥ 4.0) are located within regions of increased Coulomb stress (~5 bars; Fig. 14 lower panels). However, some aftershocks – particularly in the Elbistan sequence (profile B-B′ profile) – occur above the fault plane, where the Coulomb stress decreases.

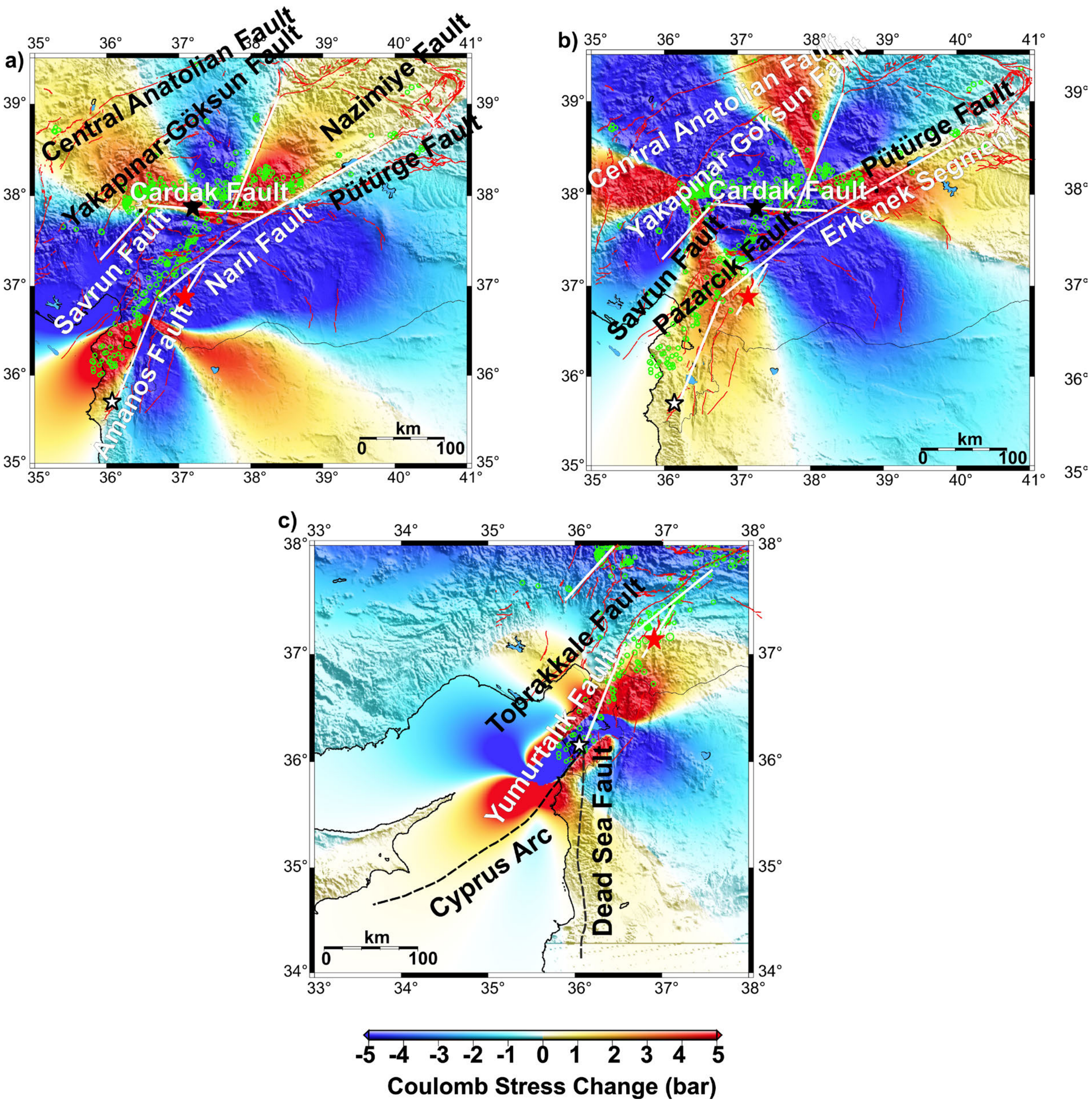

Figure 13. Coulomb stress changes, associated with the four main events (Mw > 6.5) of the 2023 Pazarcık-Elbistan earthquake sequence. The color scale ranges from −5 to +5 bar, with red indicating positive stress changes and blue indicating negative stress changes. Colored lines represent coseismic rupture segments based on the calculated strike, dip and rake of focal mechanisms and stress tensor inversions. Rupture dimensions are scaled according to earthquake magnitude (Leonard, 2010). Green circles denote Mw ≥ 4.0 aftershocks of the Pazarcık-Elbistan seismic sequence from 6 February 2023 to 27 September 2024.

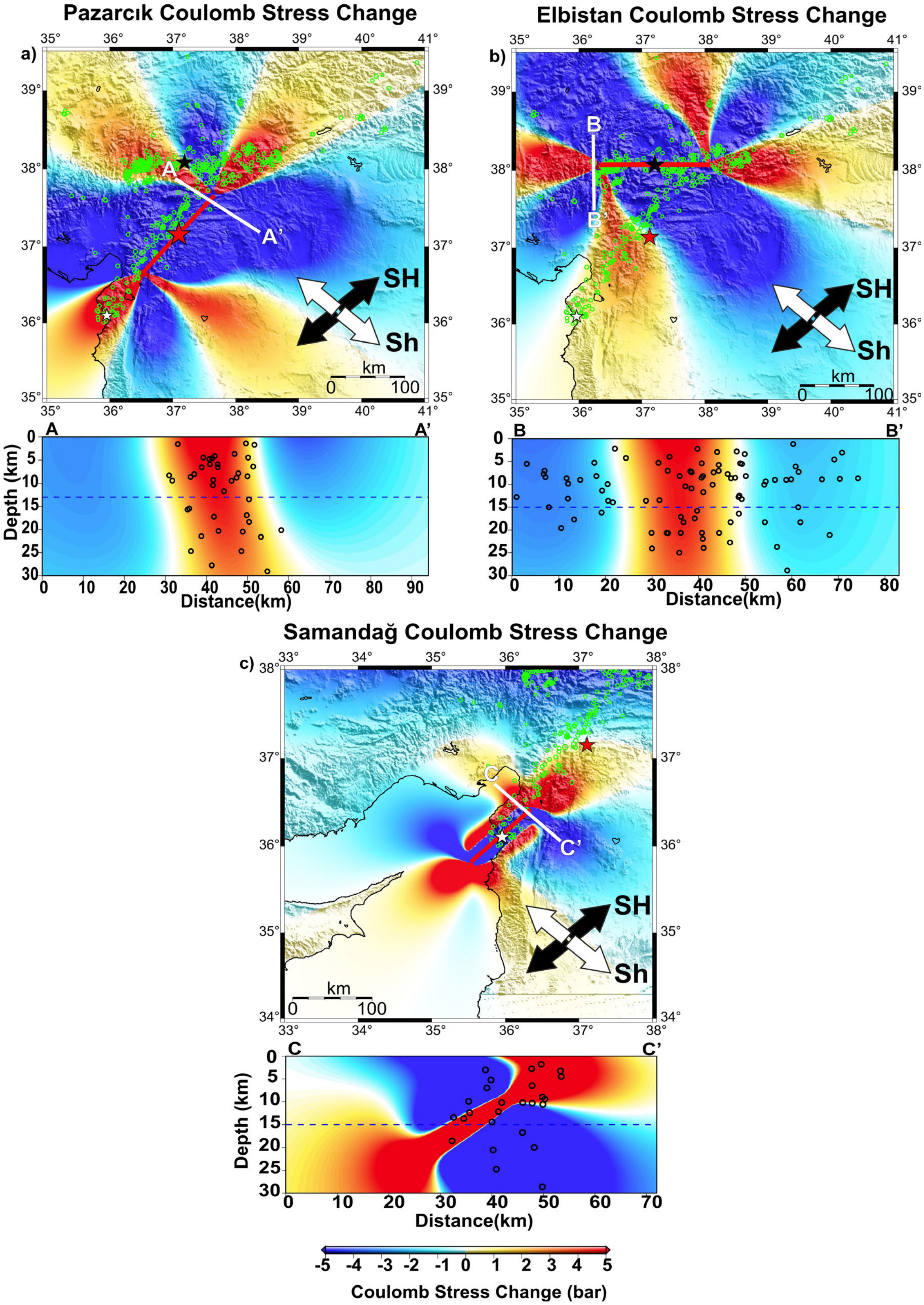

Figure 14. Cross-sections of Coulomb stress distribution for the Pazarcık Mw7.7 EQ (a), Elbistan Mw7.6 (b) and Samandağ Mw6.4 EQ (c). Profiles are shown in the upper bird-view maps. Red line highlights coseismic ruptures of the mainshocks according to fault geometry based on this study (Table 2 and Table 3). Empty circles represent earthquake hypocenters ML > 4.0 (bottom side). The size of the empty circles is proportional to magnitude. Black and white arrows display the maximum (SH) and minimum (Sh) horizontal compressive stress from the stress tensor inversion results, respectively.

6. Discussions

The 2023 Pazarcık and Elbistan mainshocks reflect a NE-SW and E-W trending left-lateral strike-slip faulting, respectively, in good agreement with the regional seismotectonic setting along the EAFZ to first order (Güvercin et al., 2022). Similar results for fault kinematics and local stress field orientations have been reported for the Pazarcık-Elbistan region based on analyses of larger magnitude events (Karabulut et al., 2023; Liu et al., 2023; Över et al., 2023). A regional left-lateral strike-slip regime dominates, reflecting the >150 mm yr^{-1} westward motion of Anatolia with respect to stable Eurasia (McClusky et al., 2000; Flerit et al., 2004; Reilinger et al., 2006; Aktuğ et al., 2016). However, at the local scale, the EAFZ comprises multiple segments where fault trends and the local stress regime vary systematically, as observed in the Çardak and Pazarcık areas (Balkaya et al., 2023; Kobayashi et al., 2024).

Areas of high coseismic slip are associated with aftershocks that are predominantly strike-slip, whereas low-slip barriers are characterized mostly by normal faulting aftershocks. Previous stress field analyses based on stress tensor inversion revealed clear stress partitioning and rotations of the local stress field following the Pazarcık-Elbistan mainshocks (Över et al., 2023). In this study we determine a total of 178 aftershock focal mechanisms for the Pazarcık-Elbistan sequence, including also smaller events (Mw < 4), using the entire recording period of the KOERI and AFAD seismic networks.

The transition between the Pazarcık Segment and the Çardak Fault coincides with the western termination of the Pazarcık rupture. The Pazarcık Segment itself exhibits predominantly strike-slip faulting, consistent with the overall behavior of EAFZ. Interestingly, the Pazarcık mainshock reflects dominantly strike-slip motion on steeply northward-dipping, E-W-trending fault plane with a normal component. Notably, larger (Mw ≥ 4) aftershocks within the Pazarcık Segment and along the Narlı Fault occurred during the first hours after the mainshock and exhibit mechanisms similar to that of the Pazarcık mainshock (Figs. 4 and 5). The Pazarcık and Elbistan ruptures involved ~9m of left-lateral surface slip along the Çardak Fault and the Pazarcık-Erkenek segments, compared to ~5m along the Amanos Segment in the south (Karabulut et al., 2023). Our results suggest that the Pazarcık mainshock, occurred along the Narlı Fault, which represents a secondary branch of the EAFZ in this area, placed the Çardak Fault under tension, promoting strike-slip faulting along the near-vertical Çardak Fault. Approximately 9 hours later, the entire Çardak Fault was activated, extending the rupture by ~50 km to the west. Figure 11a shows the spatial distribution of faulting types across the Pazarcık-Elbistan region. Two dominant faulting styles are observed: strike-slip faulting in the southern part of the region and normal faulting in the northern part. Overall, focal mechanisms along the EAFZ indicate predominantly left-lateral strike-slip motion, with a secondary contribution from normal faulting.

The focal mechanisms analyzed in this study have residuals < 0.4 and high confidence levels, as they were derived from a local seismic network with good azimuthal coverage (Table 2, Fig. 2). The resulting β values (≤33°) for the individual clusters are sufficiently low to support a relatively homogeneous and uniform stress field within the different areas (ÇC, DC, SC, EC, PC and AC) (Vavryčuk, 2014; Table 3). The DC, PC and AC subsets exhibit slightly higher β values than the other clusters (ÇC, SC and EC), but overall show very similar stress field orientations. The analyzed volumes have β values low enough to satisfy the criterion for relatively homogeneous data sets and do not indicate a first-order dependence of stress field homogeneity on rupture size or confining pressure down to ~25 km depth (Fig. 11b). High variance, or high β, reflects a poor fit of a homogeneous stress tensor to the observed focal mechanisms and therefore indicates strong stress field heterogeneity (Michael et al., 1990; Gillard et al., 1996; Lu et al., 1997; Wiemer et al., 2002; Görgün et al., 2010).

Karabulut et al. (2023) and Över et al. (2023) observed that aftershocks focal mechanisms in this region are highly diverse, indicating a strongly heterogeneous stress field that may have been partly generated during rupture of the Pazarcık-Elbistan mainshocks. Such heterogeneity may promote the formation or reactivation of complex fracture networks outside the main rupture zones, including so-called secondary faults or segments. Additionally, average fast polarization directions derived from ray paths propagating within the EAFZ, south of the Amanos Segment and Hatay Basin, are neither aligned with the local fault strike nor with the expected regional maximum compressive stress direction. The pronounced spatial variability of these observations suggests that multiple structures and mechanisms contribute to the observed crustal anisotropy in this region (Abdelmeguid et al., 2023).

Wiemer et al. (2002) proposed a heterogeneous stress field hypothesis, whereby mainshocks redistribute stress in their immediate vicinity. It is therefore reasonable to assume that stress is significantly modified – and generally reduced – near the rupture zone. The complex slip distribution during the two mainshocks leads to heterogeneous stress redistribution along and around the activated fault segments. This, in turn, results in locally variable focal mechanisms and, in part, high stress field variance. Wiemer et al. (2002) and Toda et al. (2011b) further suggested that such stress heterogeneity can produce large variations in Coulomb stress, as numerous small faults with different orientations may be activated. In this study, however, the stress field appears more heterogeneous in regions where mean Coulomb stress values exceed ~4 bars, particularly to the north, west and south of the EAFZ (Fig. 14). The Pazarcık-Elbistan rupture terminated at the Savrun Fault and did not propagate further west. Our results do not fully support the hypothesis of Wiemer et al. (2002), which correlates high Coulomb Stress values directly to increased stress heterogeneity. At present, we cannot fully explain the apparent correlation between low β values and high Coulomb Stress variances north, south and west of the Pazarcık-Elbistan rupture zone. This discrepancy may be related either to rupture dynamics or to pre-existing crustal heterogeneities. The predominant orientation of the EAFZ in this region is approximately N40°E, extending for about 180 km (including Palu, Pütürge, Erkenek and Pazarcık segments) and dipping ~55° to the north. This segment accommodated up to ~9 m of right-lateral coseismic slip during the Pazarcık-Elbistan mainshocks (Kürçer et al., 2023).

In this study, the number of aftershock focal mechanisms in the Pazarcık-Elbistan sequence has been substantially increased, allowing further subdivision of the Çardak Fault (Table 3) and the identification of local variations in stress field orientation. Left-lateral strike-slip faulting is observed along the Çardak Fault. Events with magnitudes ranging from 3.7 to 7.7 occur at depths of 1.5-28 km, corresponding to the down-dip extension of the surface trace of the fault (Fig. 14). For the Çardak Fault, the orientation of $\sigma1$ is N203°E with a plunge of 15°. No surface ruptures were observed west of Çardak Fault, near the Savrun Fault, following the Elbistan earthquake, indicating that the rupture terminated in the Göksun District (Parlak et al., 2023). The westernmost segment of the Elbistan rupture affected a small portion of the E-W-trending fault bounding the Göksun pull-apart basin (Çardak Fault), with limited slip (on the order of several centimeters) that diminishes westward. Notably, the surface rupture associated with the Elbistan earthquake follows the southern boundary of the Çardak Fault, reactivates the terminal segment of the rupture, and generates additional ruptures along the western part of the fault (He et al., 2023; Xu et al., 2023; Kobayashi et al., 2024; Softa et al., 2024; Fig. 13). The ~9-hour delay between the Pazarcık and Elbistan earthquakes further highlights the time-dependent nature of the rupture process.

The hypocenter catalog of Pazarcık-Elbistan aftershocks indicates a sharp westward termination of seismic activity at the western end of the Elbistan rupture, coinciding with regions of elevated Coulomb stress values (>4 bar; Fig. 14). Afterslip appears to have extended northwest of the Pazarcık rupture (along the Çardak and Savrun faults), potentially contributing to the triggering of the Mw7.6 Elbistan earthquake on 6 February 2023, which extended the rupture about 100 km further west (Figs. 6 and 14). The Elbistan mainshock likely initiated along the Çardak Fault, possibly on the down-dip extension of the Sürgü Fault. Analysis of the CMT solution calculated from the seismological data collected by KOERI suggests a dip angle of 79° N for the Elbistan rupture (Figs. 4 and 5, Table 2), while the CMT from AFAD data indicate a slightly lower dip of ~73°N. The Elbistan epicenter is located ~6 km north of the Çardak Fault (Fig. 1c), consistent with the inferred fault geometry (strike 359°, dip ~79°N) and hypocentral depth (~12.7 km) (Table 2). The rupture propagated westward along the Çardak Fault and southward, partially reactivating the westernmost Savrun Fault (Softa et al., 2024). The maximum principal stress orientations derived in this study indicate a subvertical NE-SW trend in the Çardak Fault region. The western boundary of the Elbistan aftershock activity suggests that the Pazarcık earthquake did not fully rupture the Çardak and Sürgü faults prior to the Elbistan mainshock occurrence (Figs. 6 and 7). A comparison of the location of the Pazarcık aftershock locations at the northwestern end of the rupture with the observed surface rupture of the Elbistan earthquake, indicates that approximately half of the Elbistan rupture zone was already seismically active ~9 hours before the mainshock (Figs. 6 and 7). The slip deficit between the Pazarcık Segment (~9 m) and the Sürgü Fault (~1 m) likely placed the Çardak and Sürgü Faults under tension, promoting E-W-oriented extensional strike-slip aftershocks at the western end of the Pazarcık rupture. This process may have contributed to the activation of these faults, which acted as an asperity prior to the Elbistan mainshock (Kobayashi et al., 2024; Figs. 4, 5 and 6).

Aftershock fault plane solutions in the Çardak Cluster are mainly associated with combined left-lateral strike-slip and normal faulting, with a NE-SW orientation of the maximum principal stress (N203°E trend, 15° plunge). Conversely, the Pazarcık Cluster is characterized by a ~N-S extensional regime indicating transtensional activity with a near-vertical orientation of the maximum principal stress (N181°E trend, 54° plunge).

Although stress rotations during the seismic cycle – particularly in association with large earthquakes – are consistent with current models of faulting kinematics, such rotations should be interpreted with caution, as demonstrated for the Landers earthquake (Townend and Zoback, 2001; Bohnhoff et al., 2006). In the Pazarcık-Elbistan region (Fig. 11a), we observe a clockwise rotation of the postseismic stress field of approximately ~65° relative to both the long-term regional and coseismic stress fields. In this sector of the EAFZ, a relatively uniform NNE-SSW-trending fault was activated during the Pazarcık mainshock. Notably, the aftershock hypocentral distribution exhibits a similar ~65° clockwise rotation relative to the local coseismic fault trend (Figs. 4 and 5). This observation suggests that the mainshock-induced stress drop led to a local reorientation of the stress field, promoting the activation of optimally oriented secondary faults (Figs. 6 and 7). We propose that this rotation of the postseismic stress field is related to variations in the orientation of the EAFZ segments with respect to the regional stress field, resulting in heterogeneous loading conditions along the fault system. In particular, stress release in the northeastern part of the rupture may have driven a progressive clockwise rotation of the static stress field, as the Çardak Fault is oriented at an angle of ~65° relative to the regional maximum principal stress ($\sigma 1$, Fig. 11a). The Mw7.6 Elbistan mainshock subsequently propagated into a region of positive Coulomb stress (Fig. 13a) produced by the Pazarcık rupture and was likely influenced by this progressively rotated stress field, as indicated by our results.

During the 2023 Pazarcık-Elbistan seismic sequence, epicenter migration was observed among the three largest earthquake (Mw > 6.0). The spatio-temporal distribution of seismicity shows that the Mw7.7 Pazarcık mainshock (6 February 04:17 GMT) was followed by the Mw7.6 Elbistan event at 10:24 GMT within the ~400 km-long rupture zone (Fig. 6). This migration appears to follow a direction of progressively increasing stress, from the northwestern part of the earthquake cluster toward the southeastern part (Fig. 14). The Coulomb stress redistribution is in agreement with this pattern, as the first two major events (Mw > 7.5) produced net stress transfer from the northwest toward the epicentral regions of subsequent large events that occurred in the southeastern portion of the rupture zone. These results suggest that the Coulomb stress transfer may help identify areas of short-term increased seismic hazard. Potential regions for future activity include the Yakapınar-Göksun Fault and the Central Anatolian Fault to the west, the Malatya-Doğanşehir Fault to the north, and the Adana Yumurtalık and Toprakkale Faults to the south.

It is important to note that the 2023 earthquakes occurred within a tectonic transition zone between the Pazarcık-Narlı and Çardak faults, corresponding to distinct segments of the EAFZ. The contrasting deformation patterns associated with the Pazarcık and Elbistan events indicate spatial heterogeneity in mechanical coupling between fault systems. The observed source mechanism distributions align with models in which variations in the stress tensor control the partitioning between strike-slip and normal faulting. The presence of systematic precursory signals in both events provides important constraints on the timescales of stress accumulation and release in this strike-slip system. Billi et al. (2024) presented compelling evidence for mechanical interactions between pre- and post-seismic activity associated with the Pazarcık-Elbistan sequence along the EAFZ. Their study documents how the 2010 Kovancılar Mw6.1 and 2020 Elazığ Mw6.7 strike-slip earthquakes initiated a decade-long sequence of seismicity culminating in the 2023 events, highlighting the role of stress transfer within similar depth ranges and seismotectonic settings. The degree of intraplate coupling appears to play a key role in modulating these interactions, with fully locked fault segments being more susceptible to triggering than partially coupled ones (Billi et al., 2024; Ying and Jiang, 2024).

Recent studies have highlighted the role of Coulomb stress transfer in the Pazarcık-Elbistan earthquake sequence. For example, Zhao et al., 2023) modeled Coulomb stress changes and identified high stress values (>4.0 bar) along the Çardak Fault following the Pazarcık earthquake. Similarly, Billi et al. (2024), Chen et al. (2024), Ren et al. (2024), and Yin and Jiang (2024) investigated the pre- and post-seismic fault dynamics associated with the Pazarcık and Elbistan events. Our findings in this study are broadly consistent with these studies. However, the present work focuses on a detailed investigation of the seismological and seismotectonic structure of the Pazarcık-Elbistan rupture zone, which is overlooked in the literature. Using data from a local seismological network, we analyze small to moderate magnitude aftershocks (Mw < 5.0) to develop a comprehensive seismotectonic model of the rupture zone. This approach integrates waveform analysis and focal mechanism solutions to better constrain local and regional stress orientations. Ongoing seismicity along the Çardak Fault indicates that the system remains active. For instance, a Mw 4.0 earthquake occurred on 24 August 2025 at 02:59 (UTC), demonstrating that secondary faults continue to rupture and that the aftershock sequence has not yet fully decayed. One of the primary goals of this study is to capture this continuing seismicity and its associated source mechanisms using broadband seismic observations, to improve our understanding of the local and regional stress evolution. These stress field models provide important insight into fault orientations and rupture processes during large earthquakes and their aftershocks, and may offer constraints on the potential occurrence of future Mw > 7.0 earthquakes along the EAFZ and its subsidiary fault systems.

Based on our observations, we propose a viscoelastic rebound mechanism to explain the temporal and spatial patterns of seismicity along the EAFZ and its associated segments. This model integrates seismological observations from KOERI and AFAD networks with seismic data from the 2023 Pazarcık-Elbistan earthquakes, framed within the context of the local crustal structure. The model assumes progressive sinistral motion of a relatively rigid crustal block beneath the EAFZ, which induces elastic deformation in the overlaying crust, as evidenced by continuous GPS measurements (Fig. 2, Aktuğ et al., 2016). This deformation reflects the gradual accumulation of strain energy within the crust. As deformation proceeds, stress builds within the system through viscoelastic coupling between the rigid block and the surrounding crustal material. The progressive transfer of stress to the fault segments eventually reaches a critical threshold, at which point the strength of the crust is exceeded, resulting in rupture along pre-existing or newly formed faults at shallow depths (Fig. 13).

The seismic energy release corresponds to the peak of viscoelastic potential energy stored in the system, marking the onset of crustal rebound. This rebound drives sinistral and/or downward motion of the rigid crustal block, accompanied by recovery of surface deformation through elastic relaxation of the upper crust. Simultaneously, vertical or lateral stresses migrating in the crust begin to rebuild as the system returns toward equilibrium. The ~9-hour interval between Pazarcık and Elbistan events provides a first-order estimate of the viscoelastic relaxation timescale. This timescale is consistent with typical estimates of crustal viscosity in fault zone environments. The cyclic nature of this process explains the observed temporal clustering of shallow crustal earthquakes in the EAFZ region, with each cycle consisting of apparent loading, rupture, and recovery phases.

The key aspects of this mechanism include the mechanical coupling between surface deformation (up to ~8.5 m along the Çardak Fault, where the Elbistan mainshock occurred, www.afad.gov.tr) and shallow seismicity through viscoelastic stress transfer, the role of crustal anisotropy in focusing stress accumulation, and the feedback between fluid flow and crustal deformation. The relatively dense crustal block acts as a stress amplifier, concentrating deformation and creating conditions favorable for repeated seismic rupture at depth. This framework provides a physical basis for understanding how patterns of seismicity and stress field evolution may serve as potential precursors to shallow crustal seismic events. Incorporating crustal heterogeneity into seismic hazard models represents an important application of this approach, particularly in regions with well documented historical and instrumental seismicity. The integration of geodetic, seismic, and geological observations offers a powerful means for unraveling the complex interactions between surface deformation and shallow seismic processes in crustal structures at the regional scale.

7. Conclusions

Fault plane solutions for Pazarcık-Elbistan aftershocks along the EAFZ were analyzed to determine deformation patterns and stress regimes. A total of 178 high reliable fault plane solutions with low misfits (<0.4), derived from Pazarcık-Elbistan aftershocks recorded by the KOERI and AFAD networks, were obtained for events with magnitude range (Mw) between 3.7 and 7.7, during the time span between 2 February 2023 and 25 November 2024. These data cover the southern segment of the EAFZ and western part of the BSZ. The focal mechanisms reveal significant spatial heterogeneity in stress redistribution across different subregions, which is generally correlated with the orientation of active faults. These results improve our understanding of the interaction between active faults geometry and localized stress fields. Stress tensor inversion identifies two dominant stress regimes: (1) a NW-SE oriented strike-slip regime along the Pazarcık, Erkenek Segments and the Çardak Faults, and (2) an E-W extensional normal faulting regime below the Hatay Basin that is bounded to the south by the Amanos Segment. At the northeastern end of the EAFZ (Palu and Pütürge Segments), we observe a high variance in stress orientations coinciding with elevated Coulomb Stress values (>4 bar). We conclude that the Çardak Fault, which hosted the Mw7.6 Elbistan (second) mainshock, was brought into a critical stress state by the Mw7.7 Pazarcık (first) mainshock and represents a left-lateral strike-slip structure similar to the Savrun Fault further to the west. The Çardak Fault was partially activated at the western end of the Pazarcık rupture but did not rupture completely until ~9 hours later, producing dominantly strike-slip events along its western segment. This behavior indicates that this portion of the EAFZ acts as a fault asperity. The observed spatiotemporal variations in the stress field have important implications for Coulomb failure stress modeling and the identification of optimally oriented faults, thereby improving local seismic hazard assessment. Additionally, the Pazarcık-Elbistan sequence provides new insights into the regional seismotectonics of the EAFZ western and southern region and may help constrain the characteristics of future large earthquakes along the fault system and adjacent seismotectonic structures in southwestern Anatolia located close to large population centers.

Data availability statement. Continuous waveforms used for centroid moment tensor (CMT) solutions are downloaded from the Kandilli Observatory and Earthquake Research Institute (http://www.koeri.boun.edu.tr/sismo/2/data-request/) and Disaster and Emergency Management Presidency Earthquake Department (AFAD) (https://tdvms.afad.gov.tr). Earthquake catalogue information is received from Kandilli Observatory and Earthquake Research Institute at URL http://www.koeri.boun.edu.tr/sismo/2/earthquake-catalog/.

Acknowledgements. We thank all members of Regional Earthquake-Tsunami Monitoring Center (RETMC) at Kandilli Observatory and Earthquake Research Institute (KOERI) and Disaster and Emergency Management Presidency Earthquake Department (AFAD) for providing the continuous seismological data used in this study. We are also grateful to Dr. Masaru Nakano for providing the waveform inversion code. All figures are generated by Generic Mapping Tools (GMT) code developed by Wessel and Smith (1998).

References

Abdelmeguid, M., C. Zhao, E. Yalcinkaya, G. Gazetas et al. (2023). Dynamics of episodic supershear in the 2023 M7.8 Kahramanmaraş/Pazarcik earthquake, revealed by near-field records and computational modeling, Commun. Earth Environ., 4, 1, 456, doi:10.1038/s43247-023-01131-7.

AFAD, Disaster and Emergency Management Presidency (2023). 06 February 2023 Pazarcık-Elbistan Kahramanmaraş, Mw: 7.7 – Mw: 7.6, Earthquake Reports, www.afad.gov.tr.

Aksoy, E., M. Inceoez and A. Koçyiğit (2007). Lake Hazar Basin: A negative flower structure on the East Anatolian Fault System, EAFS, SE Turkey, Turk. J. Earth Sci., 16, 3, 319-338.

Aktuğ, B., H. Özener, A. Doğru, A. Sabuncu et al. (2016). Slip rates and seismic potential on the East Anatolian Fault System using an improved GPS velocity field, J. Geodyn., 94-95, 1-12, doi:10.1016/j.jog.2016.01.001.

Altunel, E., M. Meghraoui, V. Karabacak, S. H. Akyüz et al. (2009). Archaeological sites (tell and road) offset by the Dead Sea Fault in the Amik Basin, southern Turkey, Geophys. J. Int., 179, 3, 1313-1329, doi:10.1111/j.1365-246X.2009.04388.x.

Ambraseys, N. N. (1989). Temporary seismic quiescence: SE Turkey, Geophys. J. Int., 96, 2, 311-331, doi:10.1111/j.1365-246X.1989.tb04453.x.

Ambraseys, N. N. and J. A. Jackson (1998). Faulting associated with historical and recent earthquakes in the Eastern Mediterranean region, Geophys. J. Int., 133, 2, 390-406, doi:10.1046/j.1365-246X.1998.00508.x.

Arpat, E. and F. Şaroğlu (1972). Doğu Anadolu Fayi ile ilgili bazi gözlemler ve düşünceler, Bull. Miner. Res. Explor., 78, 78, 44-50.

Balkaya, M., H. S. Akyüz and S. Özden (2023). Paleoseismology of the Sürgü and Çardak faults-splays of the Eastern Anatolian Fault Zone, Türkiye, Turk. J. Earth Sci., 32, 3, 402-420.

Billi, A., F. Corbi, M. Cuffaro, B. Orecchio et al. (2024). Seismic slip channeling along the East Anatolian Fault illuminates long-term supercycle behavior, Nat. Commun., 15, 1, 8921, doi:10.1038/s41467-024-53234-0.

Bird, P. (2003). An updated digital model of plate boundaries, Geochem. Geophys. Geosyst., 4, 3, 1027, doi:10.1029/2001GC000252.

Bohnhoff, M., H. Grosser and G. Dresen (2006). Strain partitioning and stress rotation at the North Anatolian fault zone from aftershock focal mechanisms of the 1999 Izmit Mw = 7.4 earthquake, Geophys. J. Int., 166, 1, 373-385, doi:10.1111/j.1365-246X.2006.03027.x.

Bott, M. H. P. (1959). The mechanics of oblique slip faulting, Geol. Mag., 96, 109-117.

Bouchon, M. (1979). Discrete wave number representation of elastic wave fields in three-space dimensions, J. Geophys. Res., 84, 3609-3614, doi:10.1029/JB084iB07p03609.

Calvi, V. S. (1941). Erdbebenkatalog der Turkei und Einiger Benaehbarter Gebiete, MTA Rep., 276.

Chen, J., C. Liu, L. Dal Zilio, J. Cao et al. (2024). Decoding stress patterns of the 2023 Türkiye-Syria earthquake doublet, J. Geophys. Res. Solid Earth, 129, 10, e2024JB029213 doi:10.1029/2024JB029213.

Emre, Ö., T. Y. Duman, S. Özalp, H. Elmacı et al. (2013). 1:250.000 Scale Active Fault Map of Turkey, General Directorate Mineral Research and Exploration, Ankara, Turkey.

Ergin, M., M. Aktar and H. Eyidogan (2004). Present-day seismicity and seismotectonics of the Cilician Basin: Eastern Mediterranean Region of Turkey, Bull. Seismol. Soc. Am., 94, 3, 930-939, doi:10.1785/0120020153.

Fichtner, A., E. Saygin, T. Taymaz, P. Cupillard et al. (2013). The Deep Structure of the North Anatolian Fault Zone, Earth Planet. Sci. Lett., 373, 109-117, doi:10.1016/j.epsl.2013.04.027.

Flerit, F., R. Armijo, G. King, B. Meyer et al. (2004). The mechanical interaction between the propagating North Anatolian Fault and the back-arc extension in the Aegean, Earth Planet. Sci. Lett., 224, 3-4, 347-362, doi:10.1016/j.epsl.2004.05.028.

Frohlich, C. (1992). Triangle diagrams: ternary graphs to display similarity and diversity of earthquake focal mechanisms, Phys. Earth Planet. Inter., 75, 1-3, 193-198, doi:10.1016/0031-9201(92)90130-N.

Gephart, J. W. and D. W. Forsyth (1984). An Improved Method for Determining the Regional Stress Tensor Using Earthquake Focal Mechanism Data: Application to the San Fernando Earthquake Sequence, J. Geophys. Res., 89, B11, 9305-9320, doi:10.1029/JB089iB11p09305.

Gillard, D., A. M. Rubin and P. Okubo (1996). Highly concentrated seismicity caused by deformation of Kilauea's deep magma system, Nature, 384, 6607, 343-346, doi:10.1038/384343a0.

Görgün, E., M. Bohnhoff, F. Bulut, G. Dresen et al. (2010). Seismotectonic settings of the Karadere-Düzce branch of the North Anatolian Fault Zone between the 1999 Izmit and Düzce ruptures from analysis of Izmit aftershock focal mechanisms, Tectonophysics, 482, 170-181, doi:10.1016/j.tecto.2009.07.012.

Görgün, E. (2013). The 2011 October 23 Mw 7.2 Van-Erciş, Turkey, earthquake and its aftershocks, Geophys. J. Int., 195, 2, 1052-1067, doi:10.1093/gji/ggt264.

Görgün, E. (2014). Source characteristics and Coulomb stress change of the 19 May 2011 Mw 6.0 Simav-Kütahya earthquake, Turkey, J. Asian Earth Sci., 87, 79-88, doi:10.1016/j.jseaes.2014.02.016.

Görgün, E. and B. Görgün (2015). Seismicity of the 24 May 2014 Mw 7.0 Aegean Sea earthquake sequence along the North Aegean trough, J. Asian Earth Sci., 111, 459-469, doi:10.1016/j.jseaes.2015.06.018.

Görgün, E., K. Kekovalı and D. Kalafat (2017). The 16 April 2015 Mw 6.0 offshore eastern Crete earthquake and its aftershock sequence: implications for local/regional seismotectonics, Int. J. Earth Sci., 106, 5, 1735-1751, doi:10.1007/s00531-016-1382-4.

Görgün, E., D. Kalafat and K. Kekovalı (2020). Source Mechanisms and stress field of the 2017 Ayvacık/Çanakkale earthquake sequence in NW Turkey, Ann. Geophys., 63, 3, SE332, doi:10.4401/ag-8194.

Güvercin, S. E., H. Karabulut, A. Ö. Konca, U. Doğan et al. (2022). Active seismotectonics of the East Anatolian fault, Geophys. J. Int., 230, 1, 50-69, doi:10.1093/gji/ggac045/6522179.

Hardebeck, J. L. and E. Hauksson (2001). Stress orientations obtained from earthquake focal mechanisms: what are appropriate uncertainty estimates?, Bull. Seismol. Soc. Am., 97, 826-842.

He, L., G. Feng, W. Xu, Y. Wang et al. (2023). Coseismic kinematics of the 2023 Kahramanmaras, Turkey earthquake sequence from InSAR and optical data, Geophys. Res. Lett., 50 17, e2023GL104693, doi:10.1029/2023GL104693.

Jackson, J. and D. McKenzie (1984). Active tectonics of the Alpine-Himalayan Belt between western Turkey and Pakistan, Geophys. J. Int., 77, 1, 185-264, doi:10.1111/j.1365-246X.1984.tb01931.x.

Kalafat, D., K. Kekovalı, Y. Güneş, M. Yılmazer et al. (2009). A catalogue of source parameters of moderate and strong earthquakes for Turkey and its surrounding area (1938-2008), Boğaziçi University Press, Kandilli Observatory and Earthquake Research Institute, Istanbul, doi:10.33677/ggianas20200100037.

Karabulut, H., S. E. Güvercin, J. Hollingsworth, A. Ö. Konca et al. (2023). Long silence on the East Anatolian Fault Zone (Southern Turkey) ends with devastating double earthquakes (6 February 2023) over a seismic gap: implications for the seismic potential in the Eastern Mediterranean region, J. Geol. Soc., 180, 3, jgs2023-021, doi:10.1144/jgs2023-021.

King, G. C. P., R. S. Stein and J. Lin (1994). Static stress changes and the triggering of earthquakes, Bull. Seismol. Soc. Am., 84, 935-953, doi:10.1785/BSSA0840030935.

Kobayashi, T., H. Munekane, M. Kuwahara, H. Furui et al. (2024). Insights on the 2023 Kahramanmaraş Earthquake, Turkey, from InSAR: fault locations, rupture styles and induced deformation, Geophys. J. Int., 236, 2, 1068-1088, doi:10.1093/gji/ggad464.

Kürçer, A., H. Elmacı, E. Özdemir, C. Güven et al. (2023). 06 Şubat 2023 Pazarcık (Kahramanmaraş) Depremi (Mw 7,7) Saha Gözlemleri ve Değerlendirmeler, MTA Genel Müdürlüğü, Rapor No. 14138, 187 s., Ankara, doi:10.17211/tcd.1354765.

Leonard, M. (2010). Earthquake fault scaling: Self-consistent relating of rupture length, width, average displacement, and moment release, Bull. Seismol. Soc. Am., 100, 1971-1988, doi:10.1785/0120090189.

Le Pichon, X. and C. Kreemer (2010). The Miocene-to-Present Kinematic Evolution of the Eastern Mediterranean and Middle East and Its Implications for Dynamics, Annu. Rev. Earth Planet. Sci., 38, 323-351, doi:10.1146/annurev-earth-040809-152419.

Lienert, B. R. E. and J. Havskov (1995). A computer program for locating earthquakes both locally and globally, Seismol. Res. Lett., 66, 26-36, doi:10.1785/gssrl.66.5.26.

Lin, J. and R. S. Stein (2004). Stress triggering in thrust and subduction earthquakes, and stress interaction between the southern San Andreas and nearby thrust and strike-slip faults, J. Geophys. Res., 109, B02303, doi:10.1029/2003JB002607.

Liu, C., T. Lay, R. Wang, T. Taymaz et al. (2023). Complex multi-fault rupture and triggering during the 2023 earthquake doublet in southeastern Türkiye, Nat. Commun., 14, 1, 5564, doi:10.1038/s41467-023-41404-5.

Lu, Z., M. Wyss and H. Pulpan (1997). Details of stress directions in the Alaska subduction zone from fault plane solutions, J. Geophys. Res., 102, 5385-5402, doi:10.1029/96JB03666.

Lund, B. and R. Slunga (1999). Stress tensor inversion using detailed microearthquake information and stability constraints: Application to Olfus in southwest Iceland, J. Geophys. Res., 104, 14947-14964, doi:10.1029/1999JB900111.

Lyberis, N., T. Yürür, J. Chorowicz, E. Kasapoğlu et al. (1992). The East Anatolian Fault: an oblique collisional belt, Tectonophysics, 204, 1-2, 1-15, doi:10.1016/0040-1951(92)90265-8.

McClusky, S., S. Balassanian, A. Barka, C. Demir et al. (2000). Global positioning system constraints on plate kinematics and dynamics in the eastern Mediterranean and Caucasus, J. Geophys. Res., 105, 5695-5719, doi:10.1029/1999JB900351.

Michael, A. J. (1987). Use of focal mechanisms to determine stress: a control study, J. Geophys. Res., 92, 357-368, doi:10.1029/JB092iB01p00357.

Michael, A. J., W. L. Ellsworth and D. H. Oppenheimer (1990). Coseismic stress changes induced by the 1989 Loma Prieta, California earthquake, Geophys. Res. Lett., 17, 9, 1441-1444, doi:10.1029/GL017i009p01441.

Nakano, M., H. Kumagai and H. Inoue (2008). Waveform inversion in the frequency domain for the simultaneous determination of earthquake source mechanism and moment function, Geophys. J. Int., 173, 1000-1011, doi:10.1111/j.1365-246X.2008.03783.x.

Nakano, M., T. Yamashina, H. Kumagai, H. Inoue et al. (2010). Centroid moment tensor catalogue for Indonesia, Phys. Earth Planet. Inter., 183, 456-467, doi:10.1016/j.pepi.2010.10.010.

Nalbant, S. S., J. McCloskey, S. Steacy, A. A. Barka et al. (2002). Stress accumulation and increased seismic risk in eastern Turkey, Earth Planet. Sci. Lett., 195, 3-4, 291-298, doi:10.1016/S0012-821X(01)00592-1.

Över, S., A. Demirci and S. Özden (2023). Tectonic implications of the February 2023 Earthquakes (Mw7.7, 7.6 and 6.3) in south-eastern Türkiye, Tectonophysics, 866, 230058, doi:10.1016/j.tecto.2023.230058.

Parlak, O., A. Yavuzoğlu, A. Bayrak, O. Karayazı et al. (2023). 06 Şubat 2023 Elbistan (Kahramanmaraş) Depremi (Mw 7,6) Saha Gözlemleri ve Değerlendirmeler, MTA Genel Müdürlüğü, Rapor No 14139, 99 s., Ankara.

Reasenberg, P. A. and R. W. Simpson (1992). Response of regional seismicity to the static stress change produced by the Loma Prieta earthquake, Science, 255, 1687-1690, doi:10.1126/science.255.5052.1687.

Reilinger, R., S. McClusky, P. Vernant, S. Lawrence et al. (2006). GPS constraints on continental deformation in the Africa-Arabia-Eurasia continental collision zone and implications for the dynamics of plate interactions, J. Geophys. Res., 111, B05411, doi:10.1029/2005JB004051.

Ren, C., Z. Wang, T. Taymaz, N. Hu et al. (2024). Supershear triggering and cascading fault ruptures of the 2023 Kahramanmaraş, Türkiye, earthquake doublet, Science, 383, 6680, 305-311, doi:10.1126/science.adi1519.

Şaroğlu, F., Ö. Emre and İ. Kuşcu (1992). Active Fault Map of Turkey, General Directorate of Mineral Research and Exploration (MTA), Eskisehir Yolu, 06520, Ankara, Turkey.

Şengör, A. M. C., N. Görür and F. Şaroğlu (1985). Strike-slip faulting and related basin formation in zones of tectonic escape: Turkey as a case study, Soc. Econ. Paleontol. Mineral. Spec. Publ., 37, 227-264.

Softa, M., F. Koçbulut, E. Akgün, E. Aksoy et al. (2024). Surface rupture during the 6th of February 2023 Mw 7.6 Elbistan-Ekinözü (Kahramanmaraş) earthquake: implications for fault rupture dynamics along the northern branch of East Anatolian Fault Zone, Turk. J. Earth Sci., 33, 1, 1-21, doi:10.55730/1300-0985.1895.

Soysal, H., S. Sipahioğlu, D. Kolçak, Y. Altınok et al. (1981). Türkiye ve Çevresinin Deprem Katalogu, MÖ 2100-MS 1900, Earthquake Catalogue of Turkey and Surroundings, BC 2100-AD 1900, TÜBİTAK Project, No. TBAG 341, 99 s.

Taymaz, T., J. A. Jackson and D. McKenzie (1991). Active Tectonics of the North and Central Aegean Sea, Geophys. J. Int., 106, 433-490, doi:10.1111/j.1365-246X.1991.tb03906.x.

Toda, S., R. S. Stein, K. Richards-Dinger, S. Bozkurt et al. (2005). Forecasting the evolution of seismicity in southern California: Animations built on earthquake stress transfer, J. Geophys. Res., 110, B05S16, doi:10.1029/2004JB003415.

Toda, S., J. Lin, M. Meghraoui, R. S. Stein et al. (2008). 12 May 2008 M = 7.9 Wenchuan, China, earthquake calculated to increase failure stress and seismicity rate on three major fault systems, Geophys. Res. Lett., 35, L17305, doi:10.1029/2008GL034903.

Toda, S., R. S. Stein and J. Lin (2011a). Widespread seismicity excitation throughout central Japan following the 2011 M = 9.0 Tohoku earthquake and its interpretation by Coulomb stress transfer, Geophys. Res. Lett., 38, L00G03, doi:10.1029/2011GL047834.

Toda, S., R. S. Stein, V. Sevilgen, J. Lin et al. (2011b). Coulomb 3.3 Graphic-Rich Deformation and Stress-Change Software for Earthquake, Tectonic, and Volcano Research and Teaching-User Guide, Open-File Report 2011-1060, U. S. Department of the Interior, U. S. Geological Survey.

Townend, J. and M. D. Zoback (2001). Implications of earthquake focal mechanisms for the frictional strength of the San Andreas fault system, Geol. Soc. Spec. Publ., 186, 13-21, doi:10.1144/GSL.SP.2001.186.01.02.

Vavryčuk, V. (2014). Iterative joint inversion for stress and fault orientations from focal mechanisms, Geophys. J. Int., 199, 69-77, doi:10.1093/gji/ggu224.

Wessel, P. and W. H. F. Smith (1998). New, improved version of the Generic Mapping Tools Released, Eos Trans., AGU, 79, 579, doi:10.1029/98EO00426.

Westaway, R. (2003). Kinematics of the Middle East and eastern Mediterranean updated, Turk. J. Earth Sci., 12, 1, 5-46.

Westaway, R. (2004). Kinematic consistency between the Dead Sea Fault Zone and the Neogene and Quaternary left-lateral faulting in SE Turkey, Tectonophysics, 391, 1-4, 203-237, doi:10.1016/j.tecto.2004.07.014.

Wiemer, S., M. C. Gerstenberger and E. Hauksson (2002). Properties of the 1999, Mw 7.1, Hector Mine earthquake: Implications for aftershock hazard, Bull. Seismol. Soc. Am., 92, 1227-1240, doi:10.1785/0120000914.

Xu, L., S. Mohanna, L. Meng, C. Ji et al. (2023). The overall-subshear and multi-segment rupture of the 2023 Mw7.8 Kahramanmaraş, Turkey earthquake in millennia supercycle, Commun. Earth Environ., 4, 1, 379, doi:10.1038/s43247-023-01030-x.

Yin, F. and C. Jiang (2024). Unraveling the preparatory processes of the 2023 Mw 7.8-7.6 Kahramanmaraş earthquake doublet, Seismol. Res. Lett., 95, 2A, 730-741, doi:10.1785/0220230413.

Yönlü, Ö., E. Altunel and V. Karabacak (2017). Geological and geomorphological evidence for the southwestern extension of the East Anatolian Fault Zone, Turkey, Earth Planet. Sci. Lett., 469, 1-14, doi:10.1016/j.epsl.2017.03.034.

Zhao, J. J., Q. Chen, Y. H. Yang and Q. Xu (2023). Coseismic Faulting Model and Post-Seismic Surface Motion of the 2023 Turkey-Syria Earthquake Doublet Revealed by InSAR and GPS Measurements, Remote Sens., 15, 3327, doi:10.3390/rs15133327.

Zoback, M. L. (1992). First and second order patterns of stress in the lithosphere: the world stress map project, J. Geophys. Res., 97, 11703-11728, doi:10.1029/92JB00132.

***CORRESPONDING AUTHOR: Ethem GÖRGÜN**,
Istanbul University-Cerrahpaşa, Department of Geophysical Engineering, Istanbul, Türkiye
e-mail: ethem.gorgun@iuc.edu.tr
© 2026 the Author(s).
Open Access. This article is licensed under a Creative Commons Attribution 4.0 International License